nature portfolio

https://doi.org/10.1038/s41592-021-01355-5

Supplementary information

Monitoring protein conformational changes using fluorescent nanoantennas

In the format provided by the authors and unedited

Supplementary Information

Monitoring Protein Conformational Changes Using Fluorescent Nanoantennas

Scott G. Harroun,[1] Dominic Lauzon,[1] Maximilian C. C. J. C. Ebert,[2] Arnaud Desrosiers,[1,3] Xiaomeng Wang,[1] Alexis Vallée-Bélisle*[1,3]

1) Laboratoire de Biosenseurs & Nanomachines, Département de chimie, Université de Montréal, Montréal, Québec, H3C 3J7, Canada

2) Chemical Computing Group ULC, Montréal, Québec, H3A 2R7, Canada

3) Département de biochimie et médecine moléculaire, Université de Montréal, Montréal, Québec, H3C 3J7, Canada

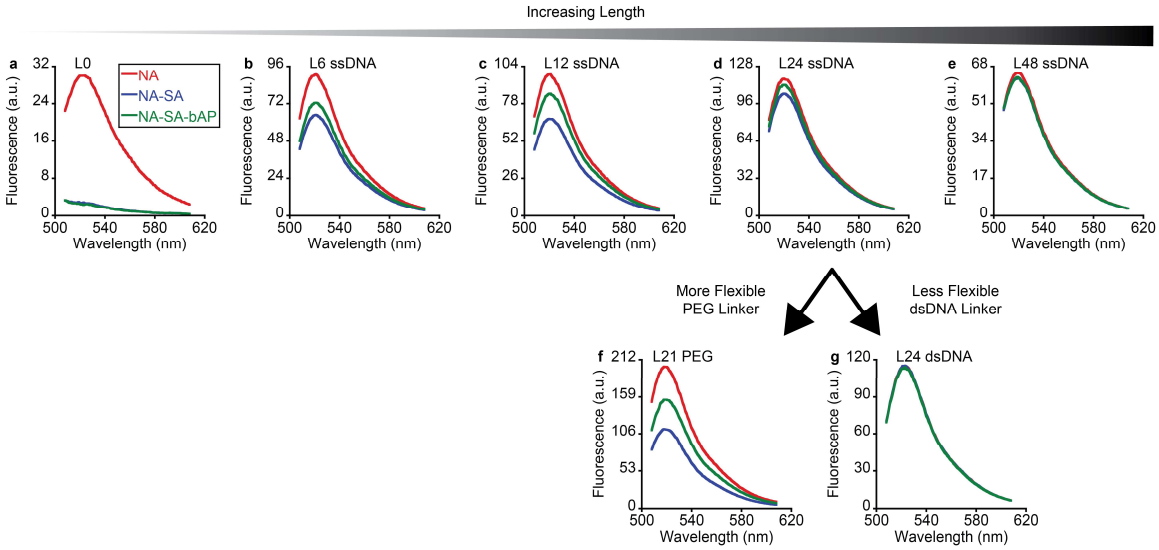

Supplementary Fig. 1. Optimal nanoantenna signaling is obtained at intermediate linker length (L12) with a flexible linker (ssDNA, PEG). These fluorescence spectra were used to generate the panels in Fig. 1. The spectra show the response of the biotinylated nanoantenna (NA) upon binding to streptavidin (SA), which quenches fluorescence, and then loading of biotinylated alkaline phosphatase (bAP), which increases fluorescence. (a) The biotin-fluorescein conjugate represents a "no linker" L0 nanoantenna, while (b) L6, (c) L12, (d) L24 and (e) L48 are ssDNA nanoantennas. The optimal linker length to monitor the assembly steps is L12. Compared to the L24, using (f) a more flexible PEG linker improves its response toward bAP, (g) while a less flexible dsDNA effectively shows no signal change. Conditions: 100 nM nanoantenna, 50 nM SA, 100 nM bAP in 200 mM Tris, 300 mM NaCl, 1 mM $MgCl_2$, pH 7.0, 37 °C.

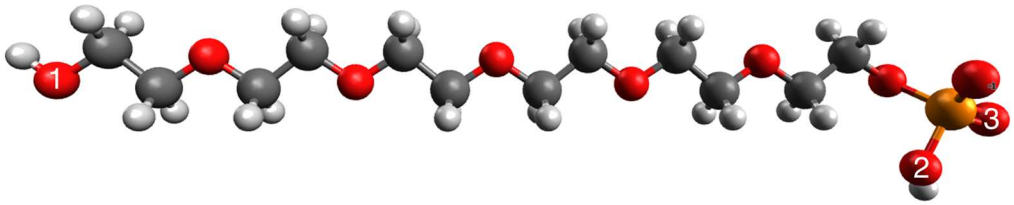

Supplementary Fig. 2. Comparison of DNA and PEG nanoantenna length. Since we compared nanoantennas based on their length in nucleotides, we wanted to determine the length of the PEG nanoantennas expressed in these units. Thus, we performed density functional theory (DFT) computations using the General Atomic and Molecular Electronic Structure System (GAMESS) via the website Chem Compute (https://chemcompute.org; This work used the Extreme Science and Engineering Discovery Environment (XSEDE), which is supported by National Science Foundation grant number ACI-1548562).[1-4] Computations used the B3LYP functional[5-8] and the 6-311++G** basis set[9-13] with diffuse functions for the negative charge. The optimized structures displayed no negative vibrational frequencies, which confirmed optimization to the ground state. We computed the length of one PEG unit produced by the Spacer 18 amidite. Thus, the molecular structure of one unit produced by Spacer 18 amidite was first drawn in Avogadro software, followed by the DFT computations. The optimized geometry was then examined in Avogadro with the Measure tool to determine its length in Å. From Point 1 to Point 2, where the next nucleotides would be located, the computed length is 21.436 Å. From Point 1 to Point 3, the maximum distance, the computed length is 23.547 Å. Based on dsDNA having a length of 3.4 Å per nucleotide,[14] one PEG unit therefore corresponds to 6.3 or 6.9 nucleotides, respectively. Since our main PEG-based nanoantenna was made from three PEG units and one unit of FAM-modified thymine (T_{FAM}), this results in a length of 19.9 or 21.8 nucleotides, respectively (note that we did not count biotin in the length of any nanoantennas since it will be buried inside streptavidin). Thus, by analogy, one could call it the *ca.* L21 PEG nanoantenna. We also used a longer PEG nanoantenna, which is made from six PEG units. It similarly corresponds to 38.8 or 42.6 nucleotides, so one could call it the *ca.* L41 PEG nanoantenna. While this comparison with DNA length is imperfect,[15] it nevertheless helps to put the maximum lengths of the nanoantennas into context.

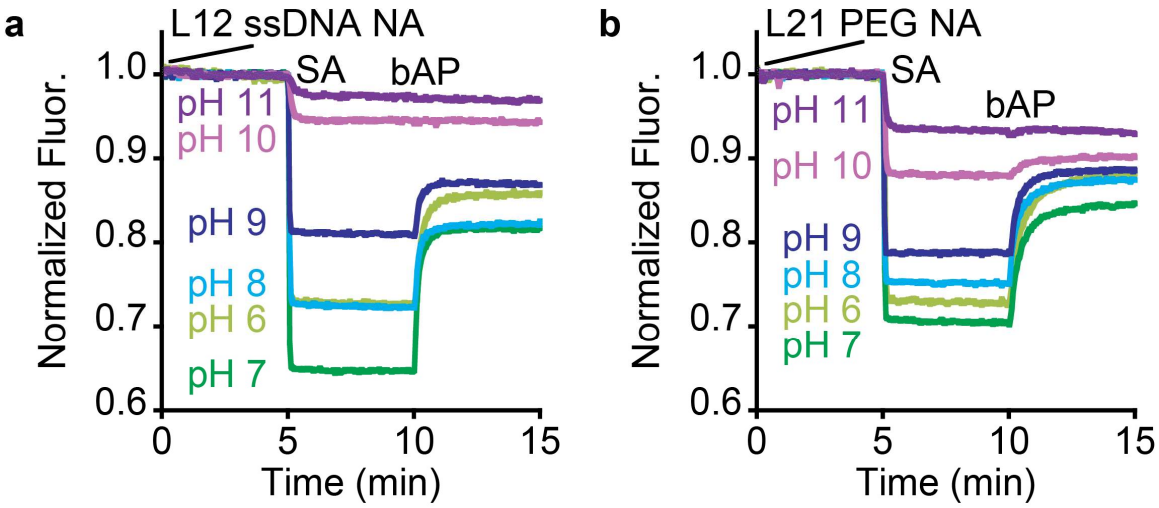

Supplementary Fig. 3. PEG nanoantennas are less sensitive to pH variation than DNA nanoantennas. The L12 ssDNA nanoantenna is less sensitive to the protein binding steps at alkaline pH, likely due to charge-charge repulsion between the negatively charged DNA linkers and proteins. The PEG nanoantenna has fewer phosphates, and therefore less negative charge. Note that the isoelectric points (pI) of SA[16, 17] and AP[18, 19] are approximately 6 and 5.5, respectively. Note also that fluorescence signal is normalized due to pH sensitivity of the FAM dye.[20] Conditions: 150 nM L12 ssDNA nanoantenna or L21 PEG nanoantenna, 50 nM SA and 50 nM bAP in 200 mM Bis-Tris (pH 6.0) or 200 mM Tris (pH 7.0, 8.0, 9.0) or 200 mM CAPS (pH 10.0, 11.0) and 300 mM NaCl (all), 37 °C.

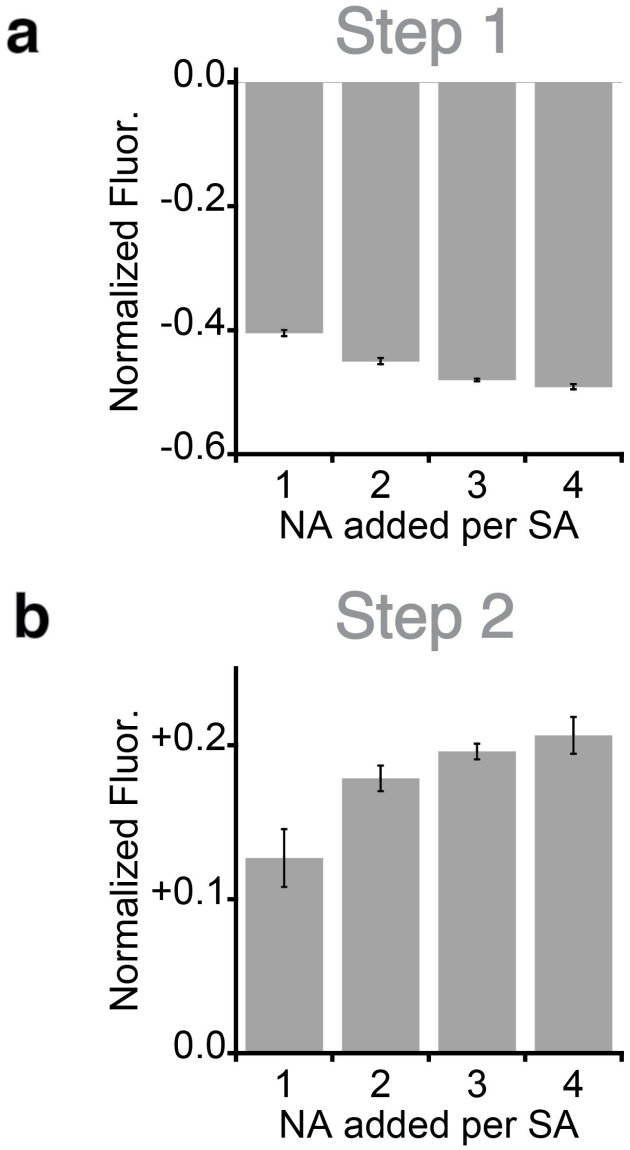

Supplementary Fig. 4. Optimization of the nanoantenna/streptavidin ratio for optimal signaling. Streptavidin (SA) has four biotin-binding sites that can bind biotinylated nanoantennas and biotinylated proteins. (a) Adding more nanoantennas per SA results in increased signal quenching. (b) Then, the signal increase upon addition of bAP is likewise greater with more nanoantennas. An important consideration, however, is that SA only has four biotin-binding sites. After addition of four nanoantennas per SA, one might expect that subsequent addition of bAP would not display a signal change because all biotin-binding sites are already full. However, this is not what we observed. Instead, the biotin-binding sites are not completely filled by the nanoantennas, likely due to steric hindrance between them.[21] We further explored the implications of the ratio of components in Supplementary Figs. 5 and 7. All experiments were performed with n=1 biologically independent enzyme samples examined over 3 independent experiments. Data are presented as mean values ± SEM. Conditions: 50, 100, 150 or 200 nM nanoantenna, 50 nM SA and 100 nM bAP in 200 mM Tris, 300 mM NaCl, 1 mM $MgCl_2$, pH 7.0, 37 °C

Note: the results in Fig. 1d-i were obtained using a nanoantenna:SA:bAP ratio of 2:1:2.

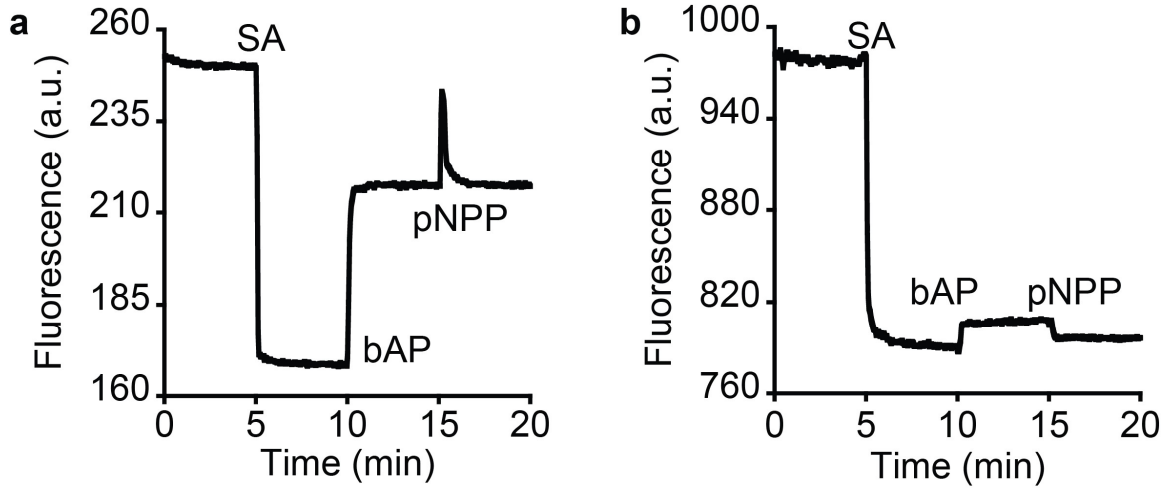

Supplementary Fig. 5. Saturating streptavidin with nanoantennas prevents bAP binding. In (a), the nanoantenna:SA ratio is 3:1, which allows for subsequent binding of bAP and detection of pNPP hydrolysis. In (b), where the ratio is increased to 12:1, the platform is saturated and cannot efficiently detect bAP and pNPP hydrolysis.

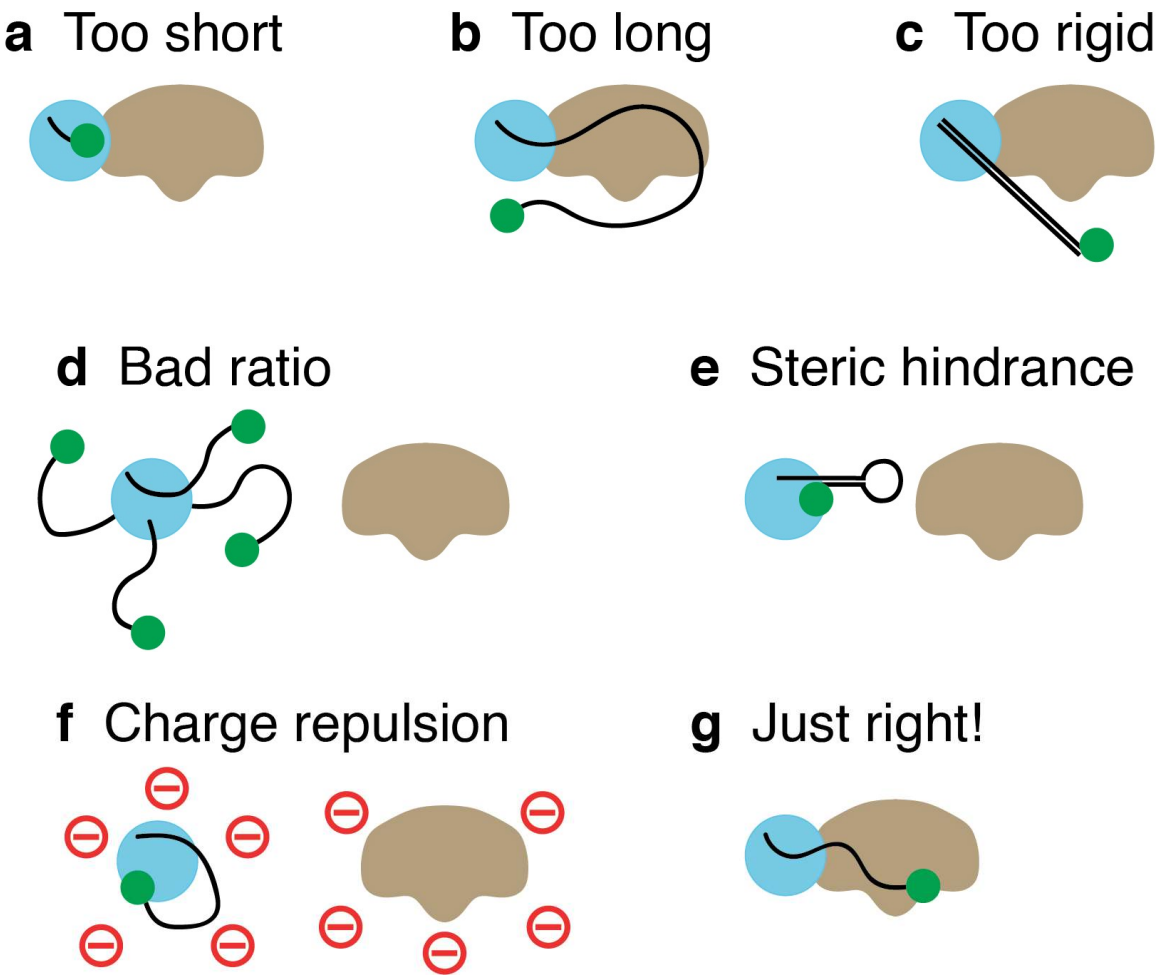

Supplementary Fig. 6. Tuning the nanoantenna linker for optimal signaling. Nanoantennas that are (a) too short, (b) too long, or (c) too rigid will prevent FAM-bAP interaction in the nanoantenna-SA-bAP complex. (d) A bad ratio of components, for example, too many equivalents of nanoantennas added per SA, will prevent bAP from binding to the nanoantenna-SA platform. (e) Likewise, steric hindrance, for example, when employing a bulky molecular beacon nanoantenna, will prevent bAP from binding to the nanoantenna-SA platform. (f) A buffer with high alkaline pH will hinder formation of the nanoantenna-SA-bAP complex due to negative charge-charge repulsion, but this can be mitigated by using PEG-based rather than DNA-based nanoantennas. (g) Representation of a nanoantenna-SA-bAP complex when the nanoantenna is optimized in terms of length, flexibility, ratio of components, etc. Note that there are likely more than one nanoantenna and bAP per SA, but one of each is shown here for simplicity.

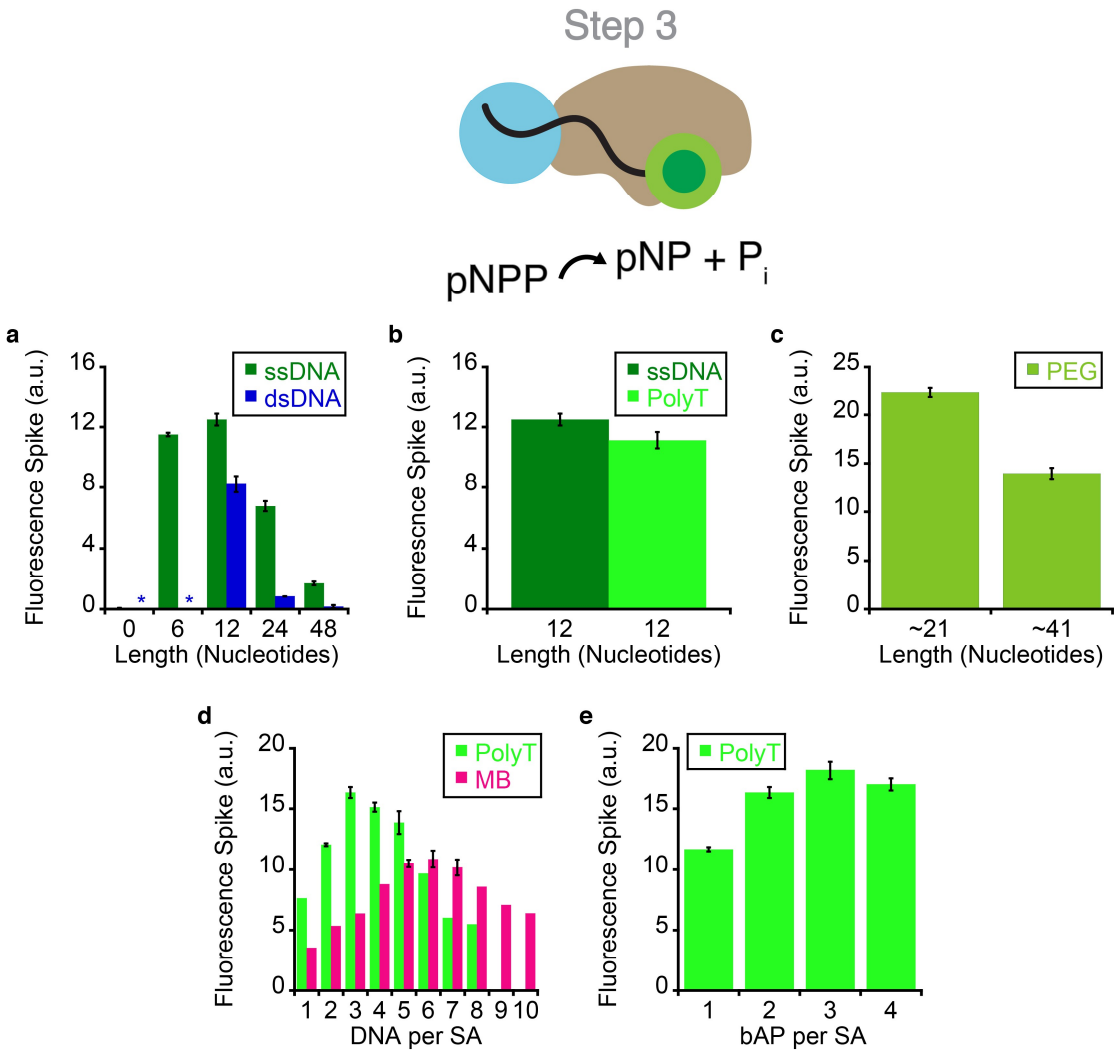

Supplementary Fig. 7. Optimal nanoantenna length, composition, and ratio for monitoring of pNPP hydrolysis. (a) The L12 ssDNA nanoantenna displays the largest spike intensity during pNPP hydrolysis. Nanoantennas that are too short (L0, L6) or too long (L24, L48) have reduced FAM-bAP interaction, and therefore, weaker signal during hydrolysis. Adding a cDNA strand (* L12, L24, L48) to form a dsDNA nanoantenna makes it too rigid for FAM to interact with bAP in most cases, although the L12 dsDNA nanoantenna still shows a good spike intensity during pNPP hydrolysis. (b) L12 ssDNA and L12 PolyT nanoantennas of equal length give similar spike intensities during pNPP hydrolysis. (c) PEG-based nanoantennas also display length dependence. (d) The spike intensity during pNPP hydrolysis depends on the ratio of nanoantennas added. The nanoantenna:SA:bAP ratio of 3:1:2 gives the best spike intensity with the L12 PolyT nanoantenna, but a bulkier 36-nucleotide molecular beacon nanoantenna requires a ratio of 6:1:2 for its optimal signal due to steric hindrance. (e) The spike intensity during pNPP hydrolysis also depends on the ratio of bAP added. The ratio of 3:1:3 is optimal, although to balance enzyme cost versus signal output, in most cases we used 3:1:2. Thus, most experiments used this ratio with concentrations of 150 nM nanoantenna, 50 nM SA, 100 nM bAP. Due to enzyme lot-to-lot variation, sometimes we used less enzyme to slow down the kinetics to have more data points per fluorescence signature (see kinetic fitting). All experiments were performed with n=1 biologically independent enzyme samples examined over 3 independent experiments. In d, only values near the maximum were in triplicate. Data are presented as mean values ± SEM. Conditions: 100 μM pNPP, 200 mM Tris, 300 mM NaCl, 1 mM $MgCl_2$, pH 7.0, 37 °C.

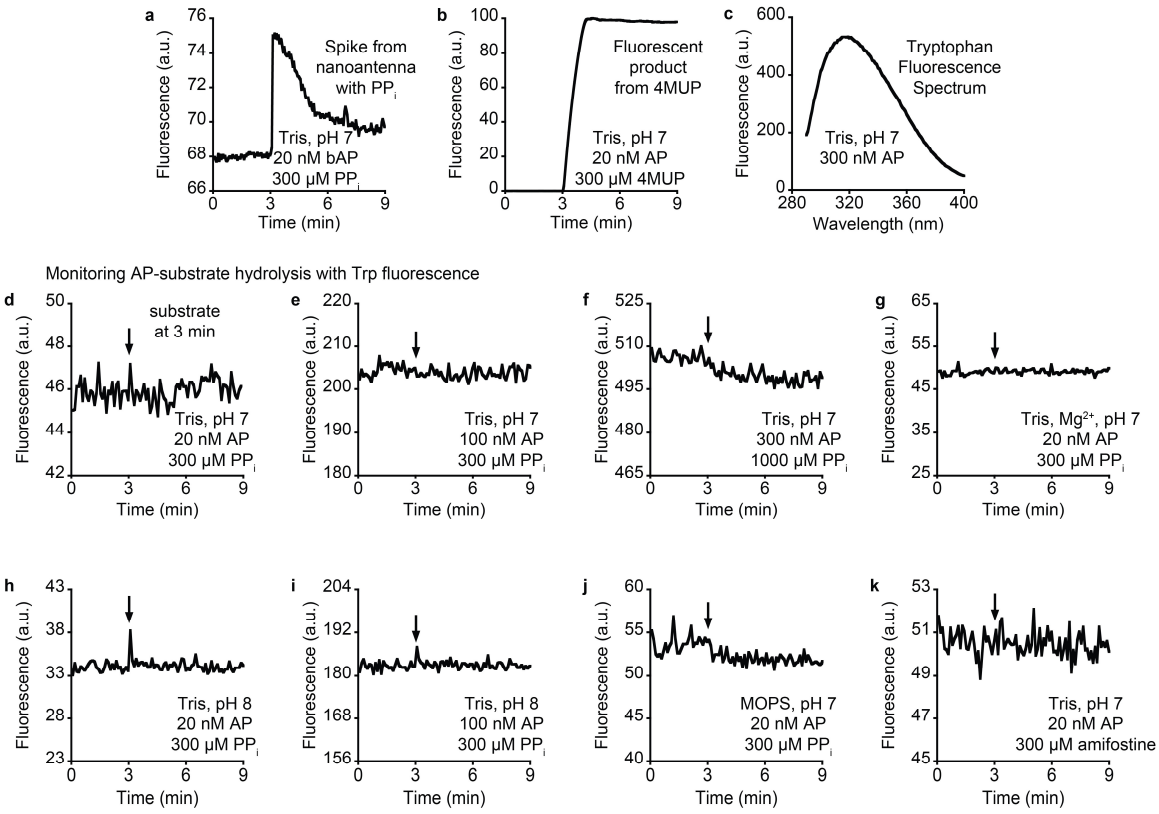

Supplementary Fig. 8. Tryptophan fluorescence does not detect AP catalytic activity. (a) PP_i hydrolysis by bAP monitored using nanoantennas and (b) 4MUP hydrolysis by AP monitored by 4MU fluorescence show that the reaction takes about 1-2 minutes. For PP_i, conditions were 150 nM nanoantenna, 50 nM SA, 20 nM bAP, 300 μM PP_i in 200 mM Tris, 300 mM NaCl, pH 7.0, 37 °C, PMT voltage = 635 V. For 4MUP, conditions were 20 nM AP, 300 μM 4MUP in 200 mM Tris, 300 mM NaCl, pH 7.0, 37 °C, PMT voltage = 400 V. (c) The AP dimer has eight Trp residues[22] and displays typical fluorescence emission when excited at 280 nm. (d-k) We tried to monitor AP function (PPi hydrolysis) using Trp fluorescence at 325 nm. Note that PP_i is ideal for this purpose because it will not appreciably absorb nor emit light. However, we found no detectable signal change under various conditions, including, (d) 20 nM AP, 300 μM PP_i in 200 mM Tris, 300 mM NaCl, pH 7.0, 37 °C, (e) 100 nM AP and 300 μM PP_i in the same buffer, (f) 300 nM AP and 1000 μM PP_i in the same buffer, (g) 20 nM AP and 300 μM PP_i in the same buffer but also with 1 mM Mg^{2+}, (h) 20 nM AP, 300 μM PP_i in 100 mM Tris, 10 mM NaCl, pH 8.0, 37 °C, (i) 100 nM AP and 300 μM PP_i in the same buffer, (j) 20 nM AP, 300 μM PP_i in 100 mM MOPS, 20 mM NaCl, pH 7.0, 37 °C, and (k) 20 nM AP, 300 μM amifostine in 200 mM Tris, 300 mM NaCl, pH 7.0, 37 °C. For Trp, PMT voltage = 800 V. The arrows indicate addition of substrate at 3 min.

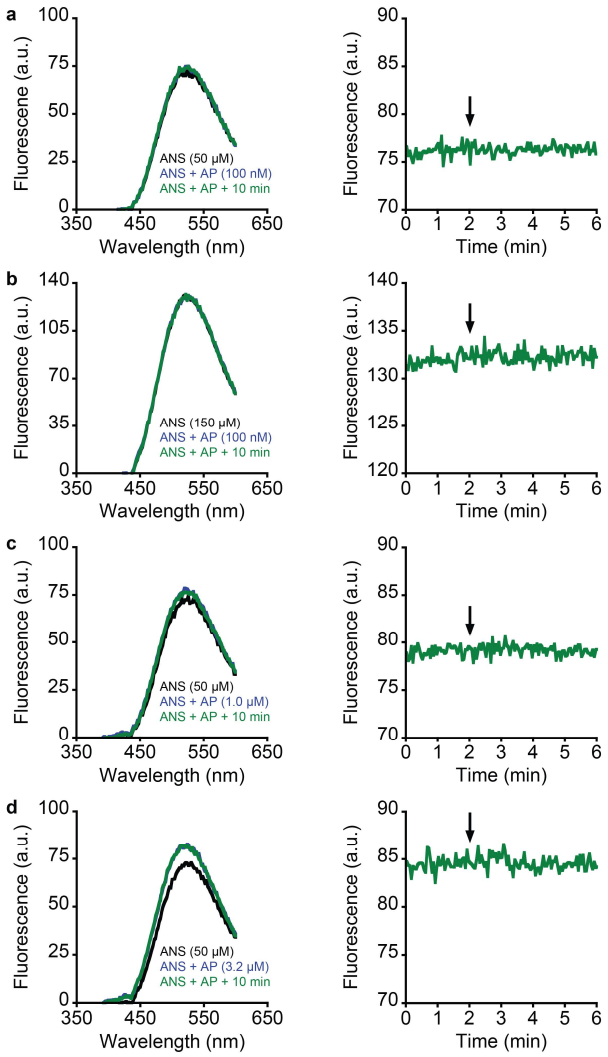

Supplementary Fig. 9. ANS probe does not detect enzyme catalytic activity. (a) Here, we tested 100 nM AP with 50 μM protein-binding dye 8-anilinonaphthalene-1-sulfonic acid (ANS). No significant fluorescence change was observed. We then tried (b) 100 nM AP with 150 μM ANS, (c) 1.0 μM AP with 50 μM ANS, and (d) 3.2 μM AP with 50 μM ANS. Adding more AP led to a small fluorescence increase. Waiting longer, up to one hour, did not lead to a further fluorescence increase. However, in all cases, this approach was not able to detect AP-mediated hydrolysis of amifostine. Note that typical ANS studies of various APs[23-27] and other proteins[28-31] have used similar concentrations of AP (or protein) and ANS. PMT voltage = 800 V, the maximum for our instrument. The arrows indicate addition of substrate at 3 min.

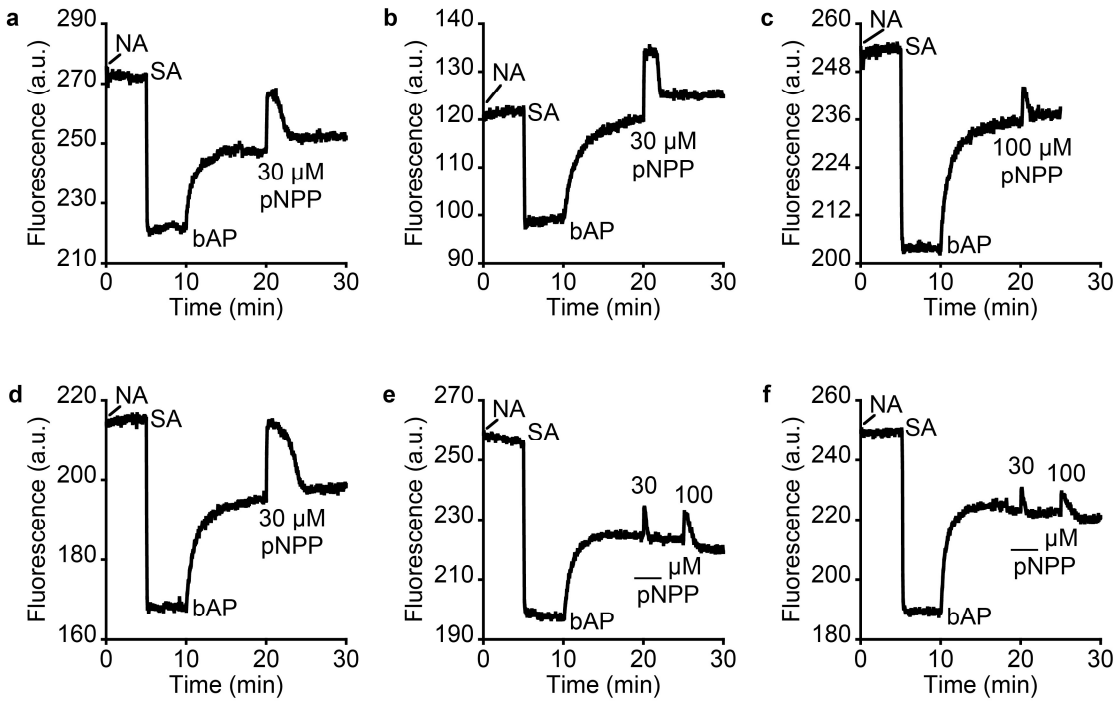

Supplementary Fig. 10. Versatility of nanoantennas in different buffer conditions. To test the versatility of our nanoantenna strategy, we tried it in different buffer conditions. (a) 100 mM Tris, 10 mM NaCl, pH 8.0; (b) 200 mM Tris, 300 mM NaCl, 1 mM Mg^{2+}, pH 7.0; (c) 200 mM Tris, 300 mM NaCl, 1 mM Mg^{2+}, pH 8.0; (d) 100 mM MOPS, 20 mM NaCl, pH 7.0; (e) 10 mM HEPES, 150 mM NaCl, 5 mM KCl, 2 mM $MgCl_2$, pH 7.45; and (f) 50 mM PIPES, 75 mM NaCl, 3 mM $MgCl_2$, pH 7.40. Note that (a-c) represent buffers used in this study, while (d-f) are randomly selected buffers found in the refrigerator of our laboratory. In all cases, we observed the binding steps and the pNPP hydrolysis spike. Conditions were 15 nM PEG nanoantenna, 2.5 nM SA, 10 nM homemade bAP and pNPP (concentration as indicated). For (c, e, f) the pNPP is quickly hydrolyzed, likely due to alkaline pH and Mg^{2+}.[32] PMT voltage = 800 V.

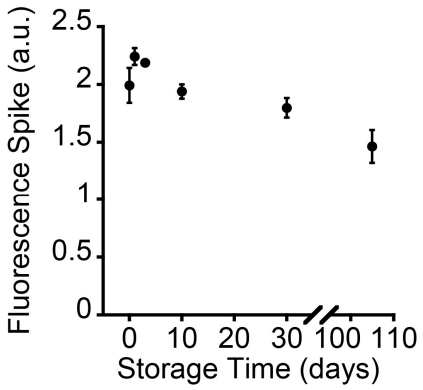

Supplementary Fig. 11. Nanoantenna-SA-bAP complex maintains functionality even after 100 days. Fluorescence spike intensity for pNPP hydrolysis as a function of storage time after preparation of nanoantenna-protein complex. Even on day 105, the signal intensity during pNPP hydrolysis remains at ~74% compared to day 0. All experiments were performed with n=1 biologically independent enzyme samples examined over 3 independent experiments. Data are presented as mean values ± SEM. Conditions: 15 nM L12 PolyT nanoantenna, 5 nM SA, 15 nM bAP and 10 µM pNPP in 200 mM Tris, 300 mM NaCl, 1 mM $MgCl_2$, pH 7.0, 37 °C. DNA-protein complex was stored in the same buffer at 4 °C. PMT voltage = 635 V.

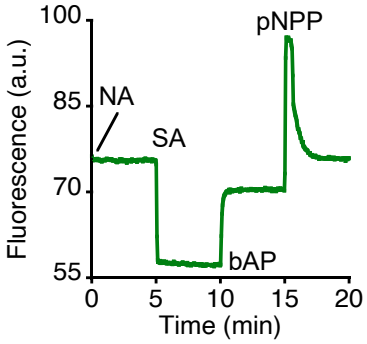

Supplementary Fig. 12. Spike above initial fluorescence baseline suggests a mechanism based on conformational change. Under some conditions, such as 3′ 5-FAM on the L12 ssDNA nanoantenna, the spike intensity during pNPP hydrolysis is higher than that of the initial fluorescence baseline before protein binding. This may support a mechanism whereby during hydrolysis the dye experiences a conformational change of nearby amino acids that increases its fluorescence, as opposed to a simple ejection from the bAP active site into the surrounding buffer. This is because ejection would likely just return the signal to the initial baseline. Conditions: 150 nM nanoantenna, 50 nM SA, 100 nM bAP and 300 μM pNPP in 200 mM Tris, 300 mM NaCl, 1 mM $MgCl_2$, pH 7.0, 37 °C.

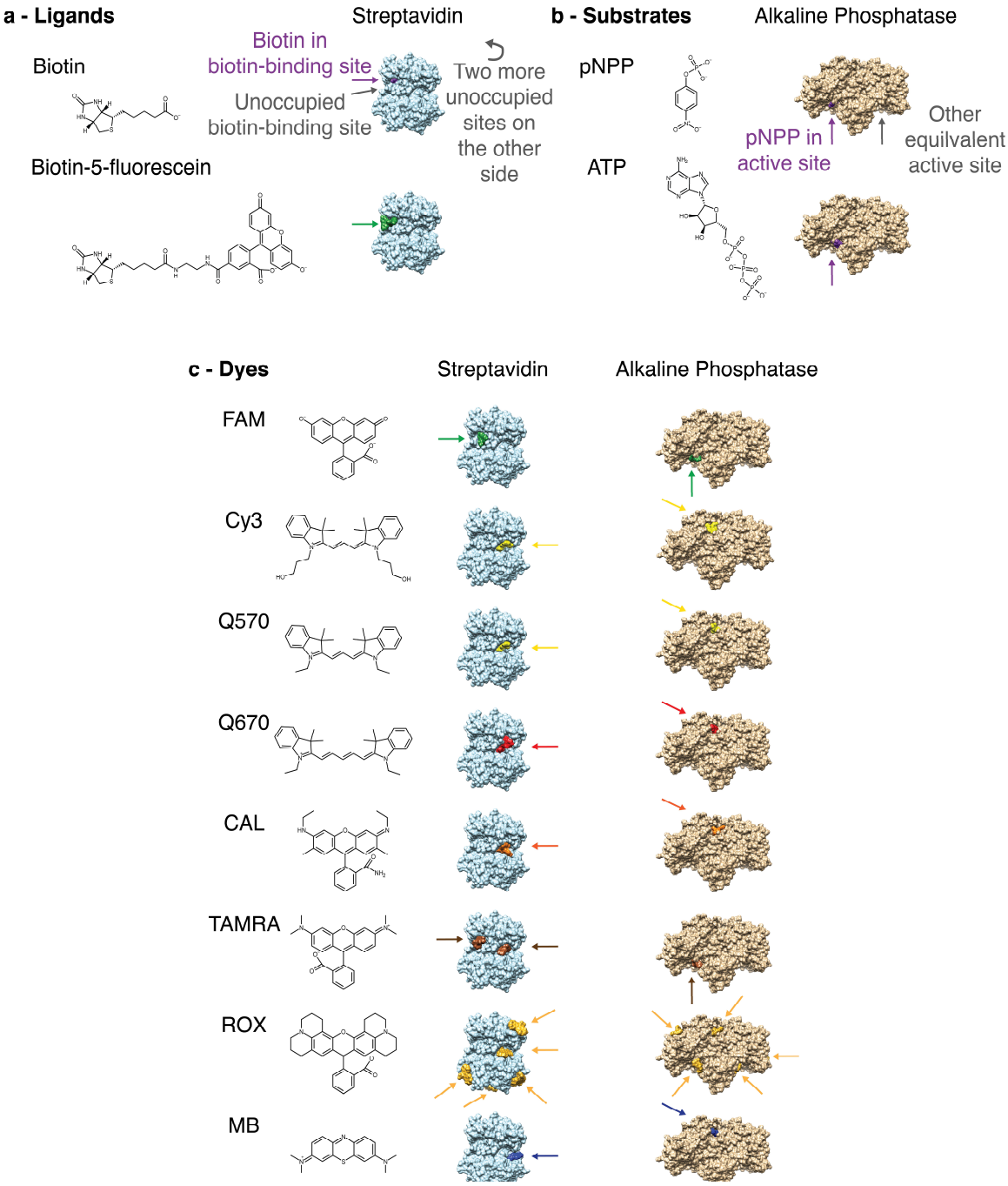

Supplementary Fig. 13. Docking of dyes and substrates with proteins. (a) The simulations predicted that biotin binds in the biotin-binding sites (BBS) of SA.[33] Likewise, biotin-5-fluorescein (L0 nanoantenna) binds with its biotin moiety in the BBS and its fluorescein moiety outside.[34] (b) The simulations predicted that the substrates pNPP and ATP bind at the active sites of AP. (c) The simulations predicted that for SA, FAM binds near the BBS,[35, 36] while Cy3, Q570, Q670, CAL, MB (methylene blue) bind in another pocket. TAMRA binds near the BBS and the other pocket in 4/10 and 6/10 jobs, respectively. For AP, FAM and TAMRA bind near the active site, while other dyes bind in a region associated with the catalytic function of mammalian APs.[37] ROX binding was not reproducible for SA and AP (examples shown). Simulations were reproducible in 9/10 or 10/10 jobs, unless noted otherwise. Molecular structures are based on the manufacturer's description, calculations in MarvinSketch software, and consideration of the literature.[38-43]

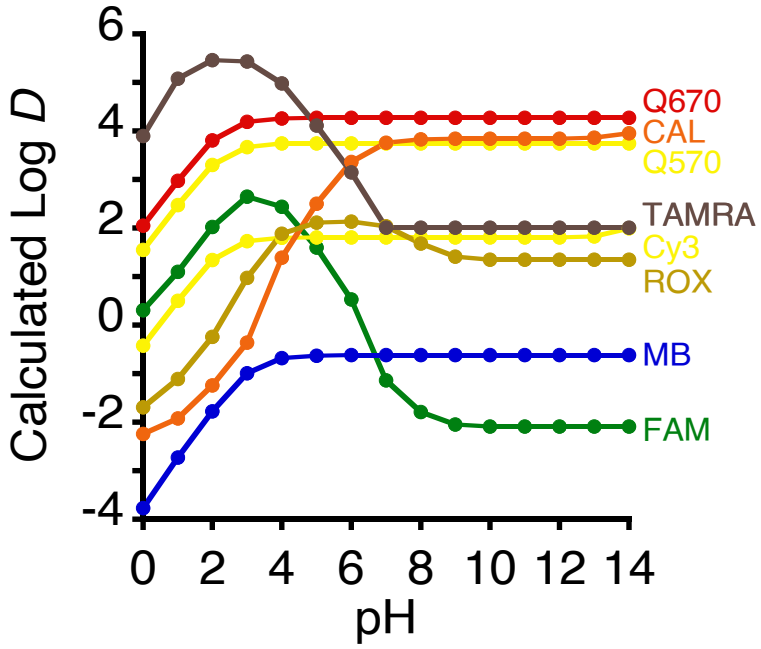

Supplementary Fig. 14. Effect of pH on dye hydrophobicity. Dye hydrophobicity as a function of pH determined by distribution coefficient (Log *D*) calculations in MarvinSketch software.[44] Log *D* values greater than zero indicate hydrophobicity, while those less than zero indicate hydrophilicity. At pH 7 or greater, only FAM and MB (Methylene Blue) are hydrophilic. Note that this approach is an approximation, as it only considers the dye itself, but not the entire nanoantenna.

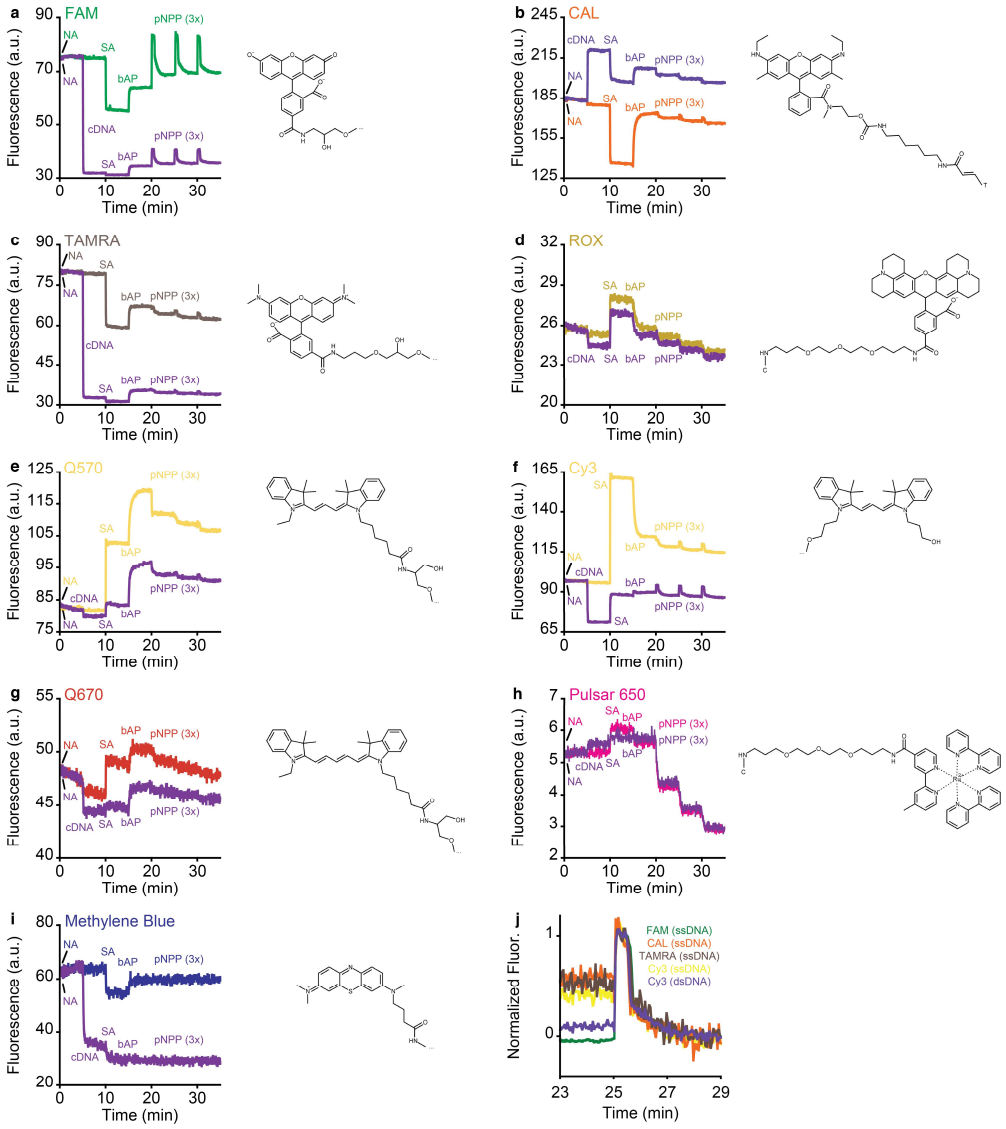

Supplementary Fig. 15. Probing different regions of the protein surface with other dyes. Kinetic signatures of nanoantennas containing (a) FAM (3′ 5-FAM), (b) CAL, (c) TAMRA, (d) ROX, (e) Q570, (f) Cy3, (g) Q670, (h) P650 and (i) MB as ssDNA (various colors) and dsDNA (purple) for SA and bAP binding and pNPP hydrolysis (3x). (j) pNPP hydrolysis monitored by FAM, CAL, TAMRA and Cy3 displays the same kinetics. For this, we selected the spike observed after the second addition of pNPP because: 1) FAM displays a different baseline after the first spike but not for subsequent spikes, and 2) for the other dyes, the first injection does not lead to a clear spike while the latter injections do. We are not sure why this difference occurs, but from the perspective of seeing whether the dyes display the same kinetics and do not act as inhibitors, this is confirmed by the second spike for each system. Conditions: 150 nM nanoantenna, 50 nM SA, 100 nM bAP and 300 μM pNPP in 200 mM Tris, 300 mM NaCl, 1 mM $MgCl_2$, pH 7.0, 37 °C. Note: FAM, TAMRA, Q570, Cy3 and Q670 are located at the 3'-end of the DNA; CAL is attached to the methyl group of a T nucleotide at the 3'-end; and ROX and P650 to the amino group of a C nucleotide at the 3'-end. MB is connected to an amino group at the 5'-end because it was borrowed from another project. Molecular structures are based on the manufacturer's description, calculations in MarvinSketch software, and consideration of the literature.[38-43]

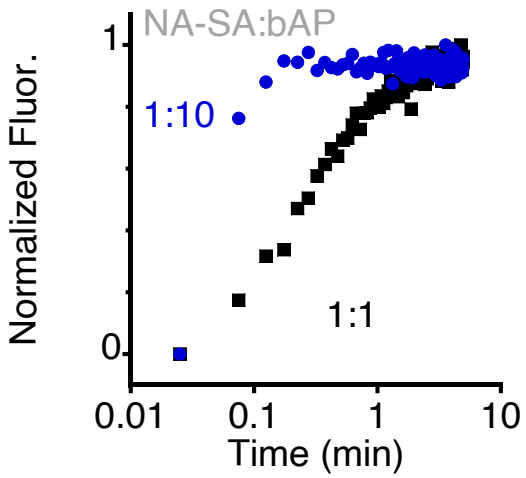

Supplementary Fig. 16. Kinetics of bAP attachment on streptavidin as monitored by FAM nanoantenna. **The rate of nanoantenna dissociation from streptavidin and subsequent binding to bAP varies with enzyme concentration, suggesting that dye dissociation is not rate-limiting.** Here, nanoantenna-SA platform to bAP ratios (NA-SA:bAP) were 1:1 or 1:10. This suggests that the rate-limiting step of this transition consists of bAP binding to SA. Ratio of bAP is relative to concentration of SA (assumed to be equal to the concentration of nanoantenna-SA platform). Conditions: 15 nM nanoantenna, 5 nM SA, 5 or 50 nM bAP in 100 mM Tris, 10 mM NaCl, 37 °C, pH 8.0. The nanoantenna was 3′ 5-FAM L12 ssDNA.

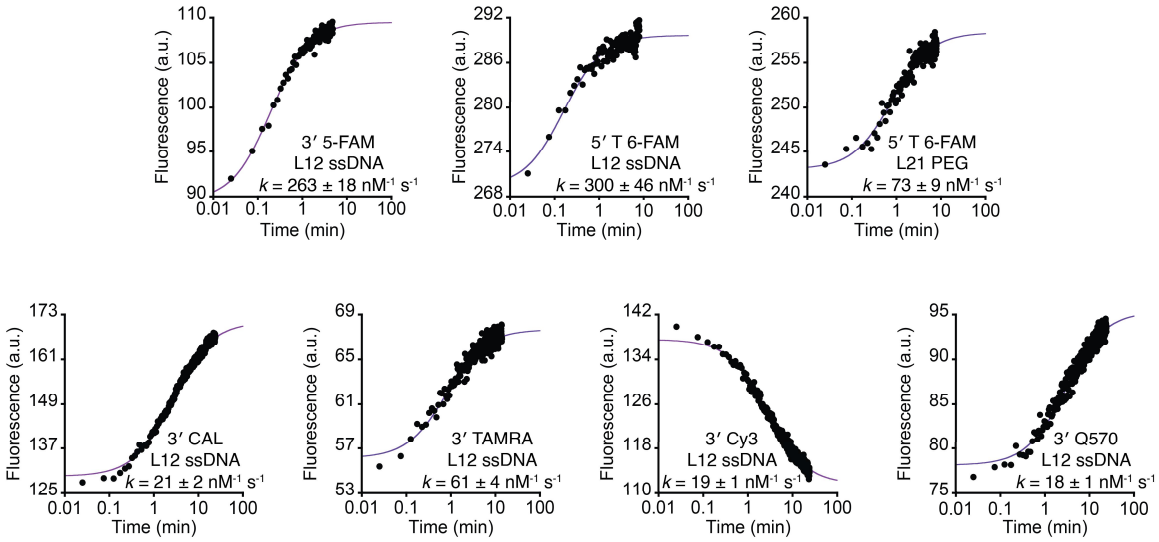

Supplementary Fig. 17. Kinetics of bAP attachment on streptavidin as monitored by different nanoantennas. The rate of nanoantenna dissociation from streptavidin and subsequent binding to bAP varies with nanoantenna properties including linker and dye. *Top row*: Changing the connection to the nanoantenna (3′ vs 5′) does not substantially affect its dissociation rate from SA and binding to bAP (263 *vs* 300 nM^{-1} s^{-1}) while changing the linker from ssDNA to PEG substantially reduces this dissociation rate (300 *vs* 73 nM^{-1} s^{-1}). *Bottom row and top left*: changing the dye (FAM, CAL, TAMRA, Cy3, Q570) substantially affects the dissociation rate of the nanoantenna from SA and binding to bAP (ranging from 263 to 18 nM^{-1} s^{-1}). The kinetics of dissociation fit well with a second-order rate constant. Conditions were equivalent to Supplementary Fig. 16 with 1x bAP. Overall, these data suggest that different nanoantennas with different dyes and/or linkers interact differently with SA, thus affecting the rate of bAP attachment likely due to steric hindrance and/or charge repulsion.

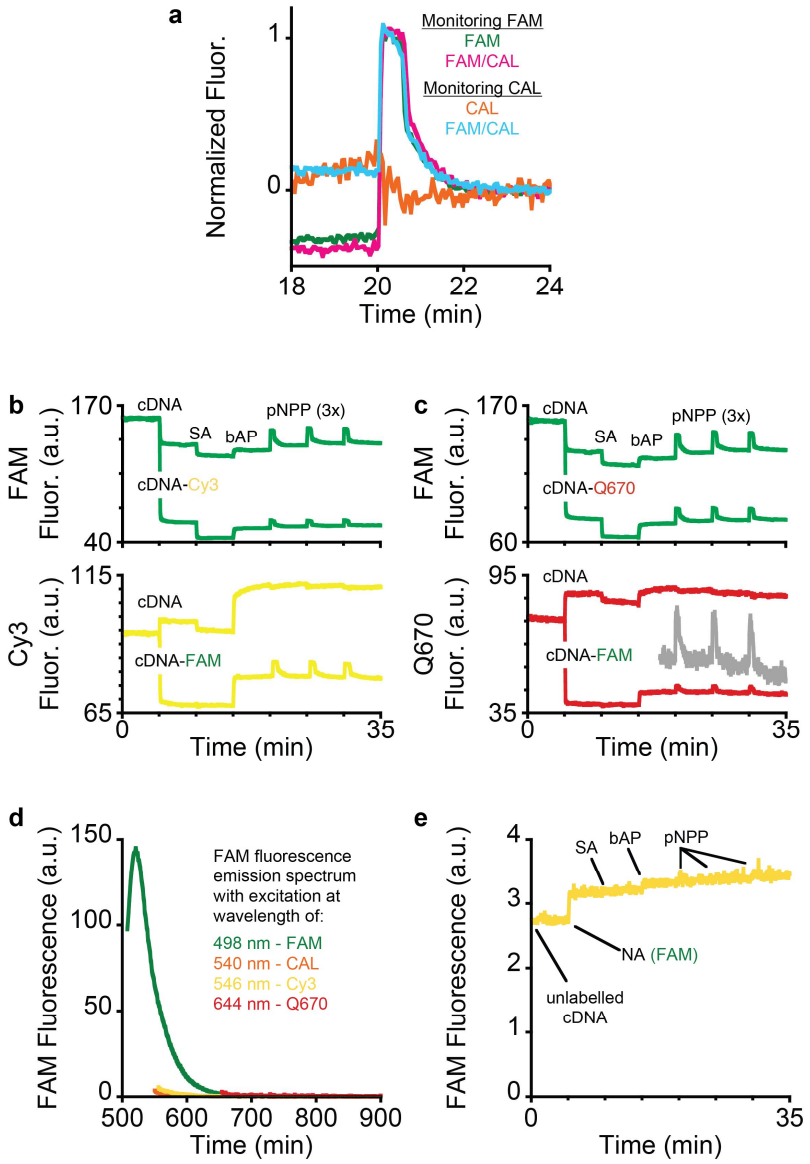

Supplementary Fig. 18. Double-dye controls. (a) pNPP hydrolysis displays the same kinetics while monitoring FAM (with or without CAL present) and while monitoring CAL (with FAM present). (b-c) Analogous experiments to the dye competition experiment in Fig. 1m-n except now with (b) FAM and Cy3 or (c) FAM and Q670. The top data shows that while monitoring FAM, the presence of the other dye does not significantly affect the FAM fluorescence signature (besides some quenching), but monitoring Cy3 or Q670 in the presence of FAM affects their fluorescence signature to the point where it is now possible to efficiently monitor pNPP hydrolysis. (d) As a control, upon excitation of FAM at 498 nm, FAM displays intense fluorescence emission at 520 nm. However, when using the excitation wavelengths optimal for CAL, Cy3 and Q670, FAM does not display fluorescence. (e) For example, in an attempt to monitor the FAM nanoantenna with the excitation (546 nm) and emission (563 nm) wavelengths of Cy3 but otherwise the same conditions, there is no substantial fluorescence emission, and it is not possible to monitor SA and bAP binding, nor pNPP hydrolysis. Conditions: 150 nM nanoantenna, 50 nM SA, 100 nM bAP and 300 μM pNPP (3x) in 200 mM Tris, 300 mM NaCl, 1 mM $MgCl_2$, pH 7.0, 37 °C.

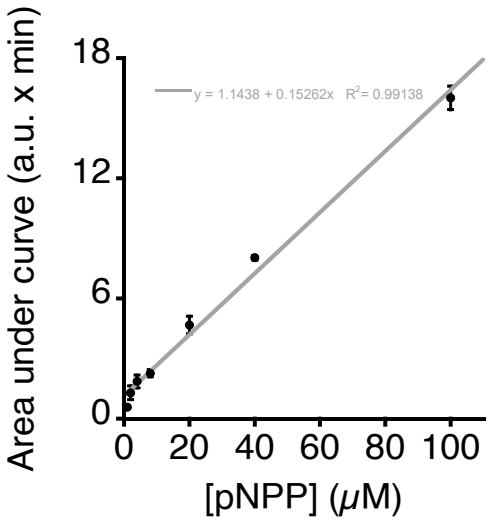

Supplementary Fig. 19. Area under spike increases linearly with pNPP concentration. Here, the fluorescence spikes in Fig. 2a were integrated with time to obtain the area under the curve (*i.e.*, the spike). The area increases linearly with pNPP concentration.

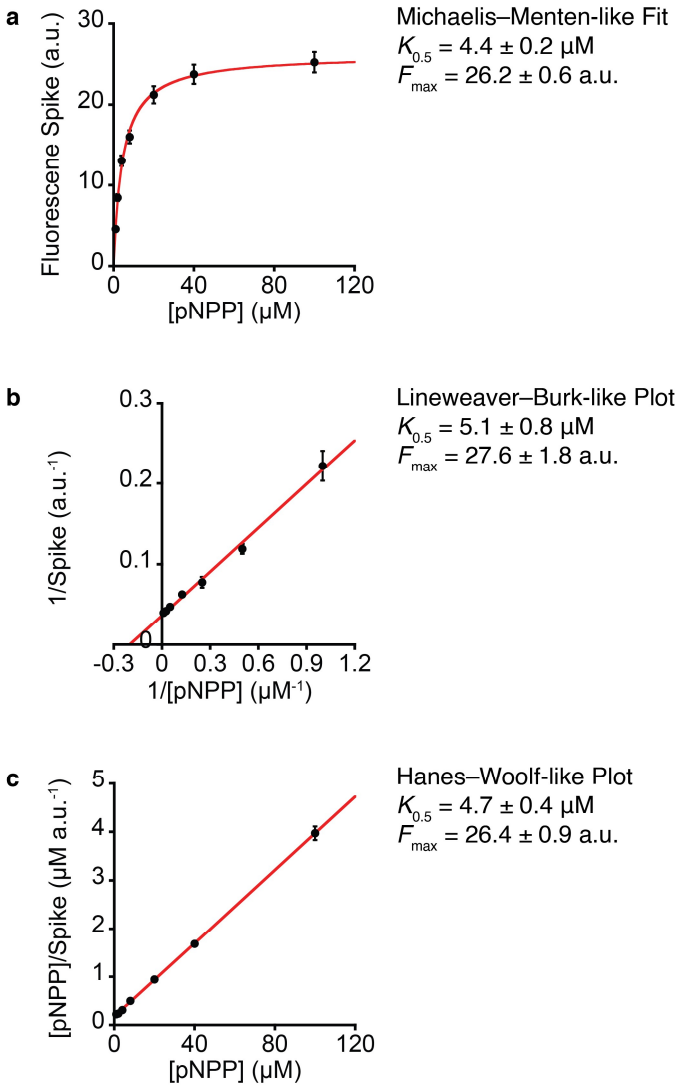

Supplementary Fig. 20. Saturation binding plot. (a) We plotted the fluorescence spike intensity for triplicate injections of 1, 2, 4, 8, 20, 40, and 100 μM pNPP. It displays Michaelis–Menten-like behavior, whereby the maximum fluorescence (F_{max}) ought to be proportional to the maximum rate (V_{max}) and enzyme-substrate concentration ([ES]). Then, the concentration at half of the F_{max} ($K_{0.5}$) ought to be equal to the Michaelis constant (K_M). Nonlinear fitting of the Michaelis–Menten equation found $K_{0.5}$ and F_{max} values, shown above. The $K_{0.5}$ agrees with the expected K_M under these conditions.[45] We show later how one can convert this fluorescence intensity to rate in μM s^{-1} (Supplementary Fig. 25). Also shown are determination of the kinetic parameters by the classic methods, (b) Lineweaver–Burk-like and (c) Hanes–Woolf-like, which provide similar numerical values. All experiments were performed with n=1 biologically independent enzyme samples examined over 3 independent experiments. Data are presented as mean values ± SEM. Conditions: 150 nM PEG nanoantenna, 50 nM SA, 100 nM bAP and variable amounts of pNPP in 100 mM Tris, 10 mM NaCl, pH 8.0, 30 °C.

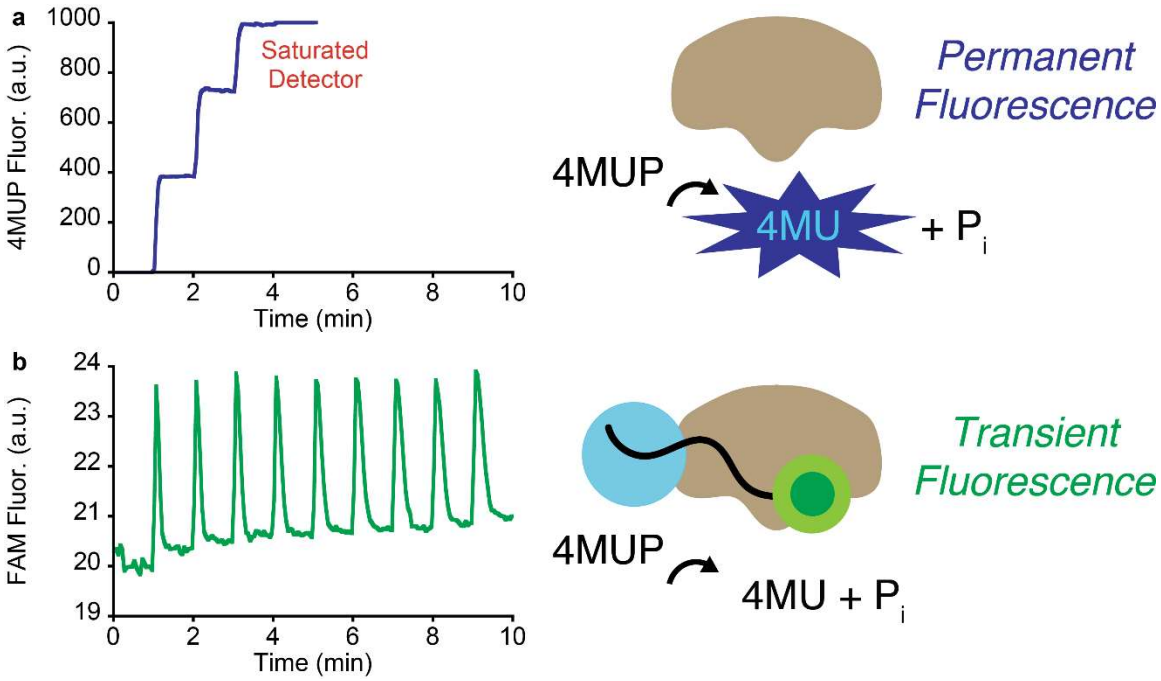

Supplementary Fig. 21. Comparison of classic assay and nanoantenna reveals that nanoantennas allow multiple analyses with the same sample. (a) Real-time fluorescence monitoring of the hydrolysis of 4MUP to fluorescent 4-MU and P_i. Although it works well for the first hydrolysis reaction (injection time = 1 min), if one desires to measure multiple injections of substrate, it will eventually saturate the detector (3 min). Note that we did not bias this experiment to fail: in most of this paper we used a PMT voltage of 635 V or higher, but in this experiment, we used 500 V, which is between the medium and low power settings on our spectrofluorometer. (b) In contrast, monitoring the hydrolysis reaction by the nanoantenna strategy allows one to perform multiple injections of substrate. Thus, the only limitation is the chemical environment of the system (*i.e.*, stability of enzyme, product inhibition), rather than a physical or instrumentation limitation. Conditions: 150 nM L12 PolyT nanoantenna, 50 nM SA, 100 nM bAP and 10 μM 4MUP (9x) in 100 mM Tris, 10 mM NaCl, pH 8.0, 30 °C.

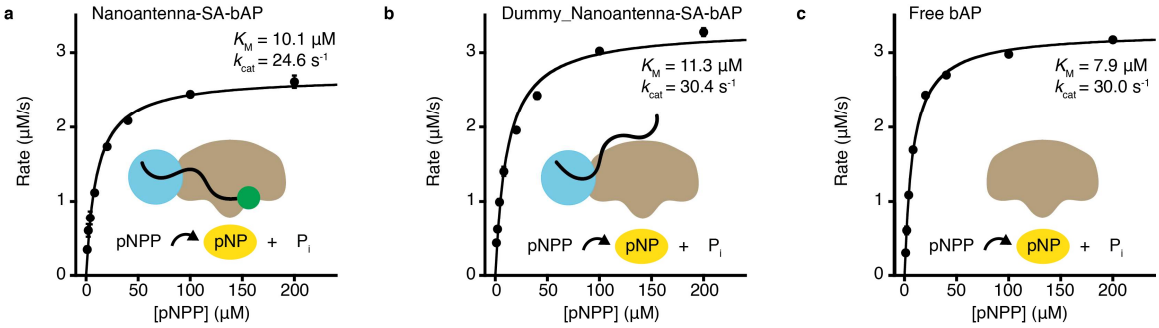

Supplementary Fig. 22. Streptavidin and nanoantennas do not affect the kinetic parameters. Michaelis-Menten kinetics as measured by UV–Vis absorbance of pNP product for (a) nanoantenna-SA-bAP complex, (b) Dummy nanoantenna-SA-bAP complex (*i.e.*, no FAM on nanoantenna), and (c) free bAP. All experiments were performed with n=1 biologically independent enzyme samples examined over 3 independent experiments. Data are presented as mean values ± SEM. Conditions: 150 nM nanoantenna, 50 nM SA, 109 nM bAP (not a typo) in 100 mM Tris, 10 mM NaCl, pH 8.0, 30 °C.[46, 47]

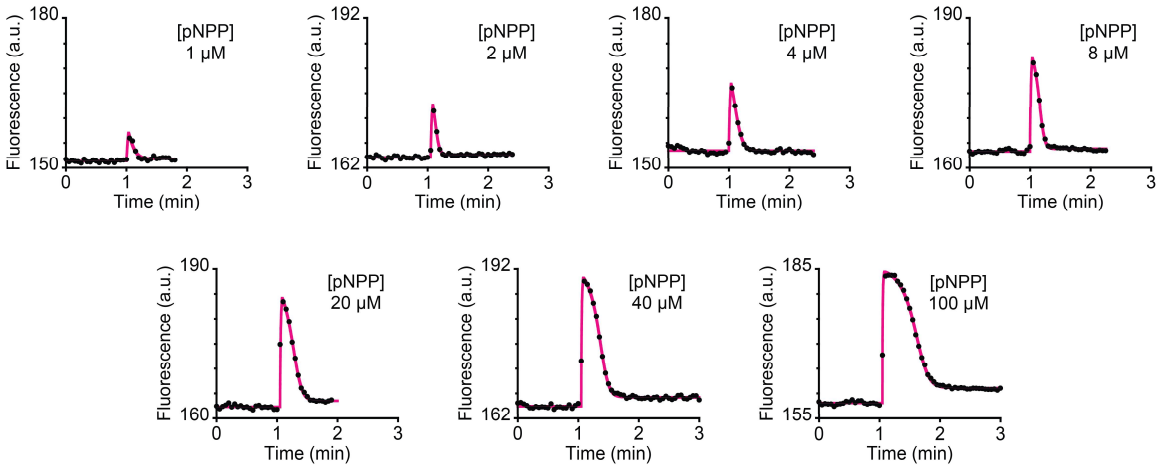

Supplementary Fig. 23. Fitting of the fluorescent spikes to extract kinetic parameters of bAP with [pNPP] = 1, 2, 4, 8, 20, 40 and 100 μM. The data are taken from Fig. 2a, and the extracted parameters are plotted in Supplementary Fig. 24.

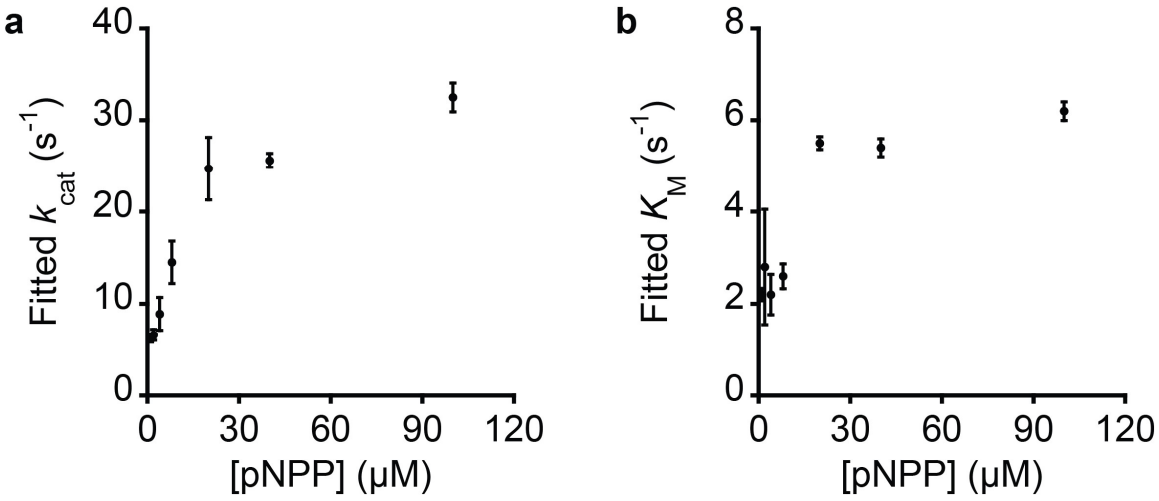

Supplementary Fig. 24. Kinetic parameters of AP determined using different concentrations of substrate (see Supplementary Fig. S23). When [pNPP] is less than ~3K_M, the extracted parameters are underestimated, and consequently unreliable, likely due to not enough enzyme-substrate complex being formed. Therefore, we recommend using a sufficiently high concentration of substrate (>3K_M) to perform the one-shot characterization fitting strategy. Also important is that these parameters for the commercially prepared bAP (20, 40 and 100 μM pNPP) are essentially the same as the parameters determined in Fig. 2d-e for our "homemade" bAP (biotinylation of AP ourselves; 30 μM pNPP), which indicates the robustness of our strategy. All experiments were performed with n=1 biologically independent enzyme samples examined over 3 independent experiments. Data are presented as mean values ± SEM.

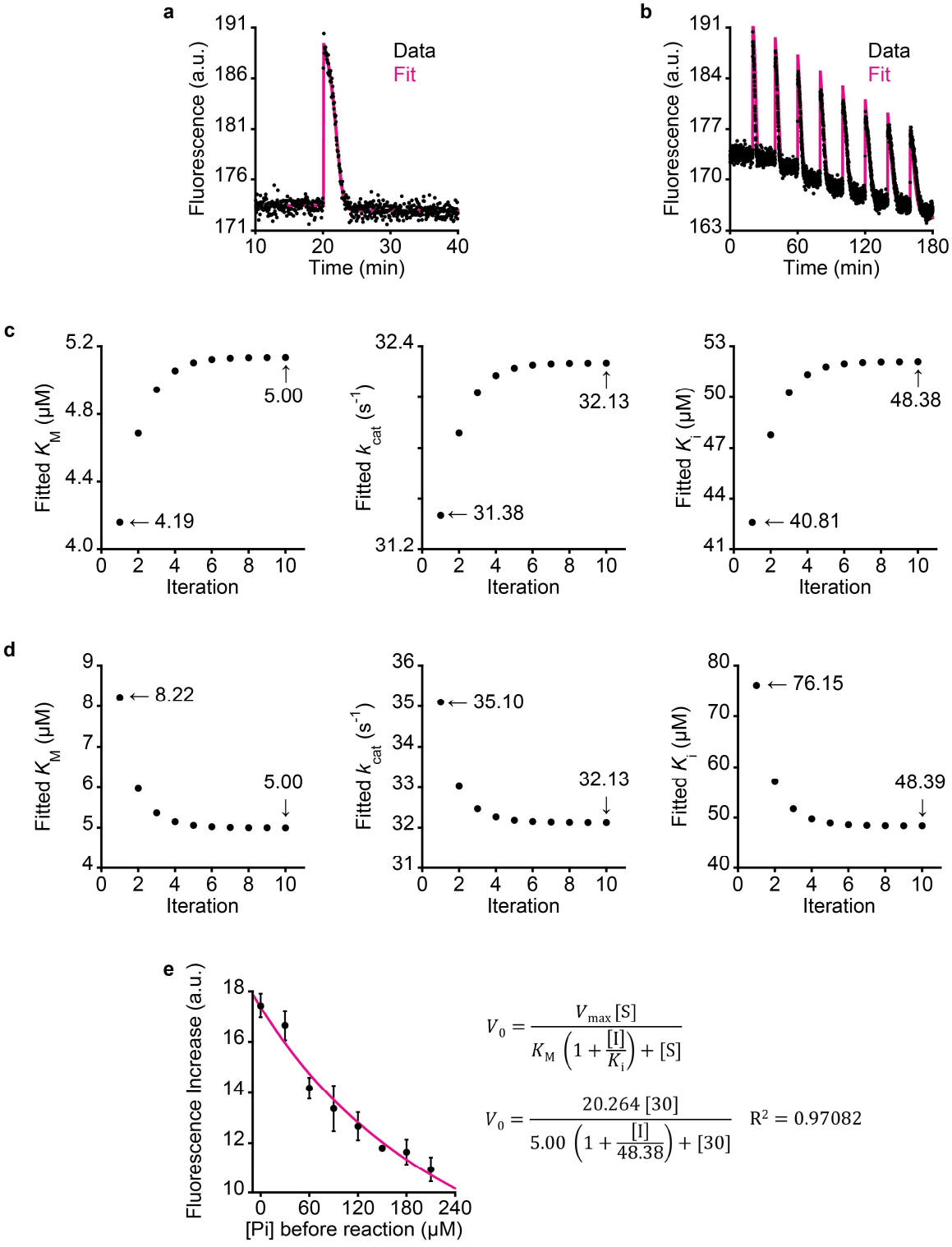

Supplementary Fig. 25. Fitting strategy employed to determine the kinetic parameters in a single experiment.[48,49] (a) A single injection of 30 μM pNPP to a cuvette containing 10 nM bAP (as nanoantenna-SA-bAP complex), overlaid with fitting in MATLAB to derive mean values of K_M = 4.19 ± 0.02 μM and k_{cat} = 31.38 ± 0.85 s^{-1}, which give k_{cat}/K_M = 7.49 ± 0.24 μM^{-1} s^{-1}. The fitting takes into consideration the product/inhibitor, P_i, so for the first calculation we used K_i = 33.7 μM, which was reported in the literature for a similar system.[45] (b) Seven more injections of 30 μM pNPP

in the same cuvette, overlaid with fitting in MATLAB using the obtained K_M and k_{cat} values to derive a mean K_i = 40.81 ± 0.95 μM for P_i. (c) Repeating the above process using the obtained K_M, k_{cat} and K_i values results in their eventual convergence. After 10 iterations of calculations, the final derived values are K_M = 5.00 ± 0.07 μM, k_{cat} = 32.13 ± 0.84 s^{-1}, k_{cat}/K_M = 6.426 ± 0.26 μM^{-1} s^{-1} and K_i = 48.38 ± 2.01 μM. (d) The literature K_i used in the initial fitting was a "good guess" and close to the determined value for our system, but if a "bad guess" had been used instead, the 10 iterations of calculations still converge to the same values. As an example, we used an initial K_i = 390 μM, as reported for bacterial AP under very different conditions.[50] With this, we still obtained the same results. (e) The spike intensity (which is proportional to the rate of the reaction) decreases with increasing inhibitor concentration (P_i). This relationship is well modeled using the Michaelis–Menten equation for competitive inhibition by employing the K_M and K_i values determined above. All experiments were performed with n=1 biologically independent enzyme samples examined over 3 independent experiments. Data are presented as mean values ± SEM. Conditions: 5 nM PEG nanoantenna, 5 nM SA, 10 nM homemade bAP and 30 μM pNPP (8x) in 100 mM Tris, 10 mM NaCl, pH 8.0, 30 °C.

See the Online Methods section as well as "Script for fitting kinetic data in MATLAB" at the end of this document.

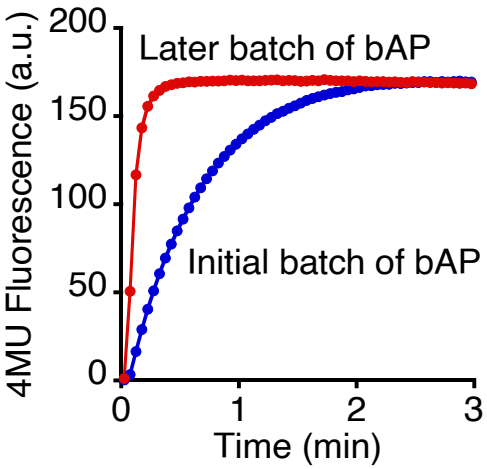

Supplementary Fig. 26. bAP batch-to-batch variation accounts for differences in kinetic parameters. The initial and later batches of bAP used in this study had different rates of substrate hydrolysis, as shown here for the conversion of nonfluorescent 4MUP to fluorescent 4MU and P_i. Thus, differences in determined K_M and k_{cat} between Fig. 2 and Fig. 3 can be attributed to the batches (different lots).

Importantly, substrate comparison (*e.g.*, Fig. 3) was done with the same enzyme lot.

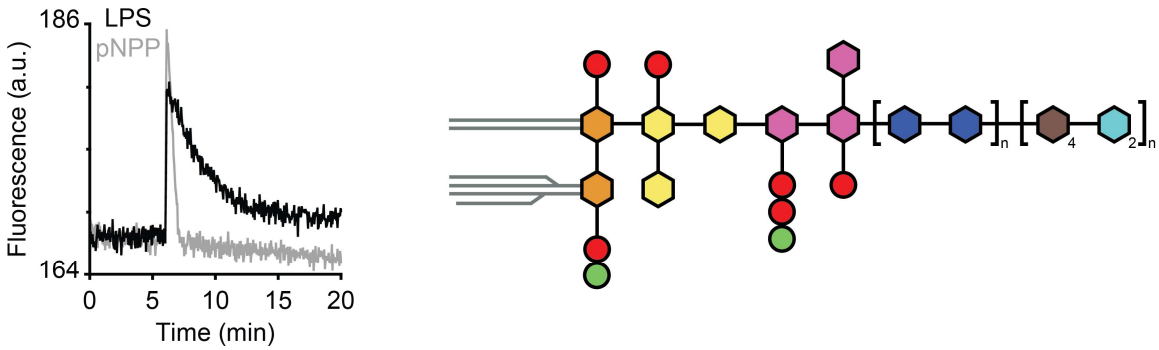

Supplementary Fig. 27. Real-time monitoring of AP function using LPS substrate. Nanoantenna fluorescence signature observed during hydrolysis of approximately 2.5 μM lipopolysaccharide (LPS) compared with 2.5 μM pNPP. Shown also is a simplified scheme of LPS structure.[51]

LPS was used at a lower concentration than the other substrates due to low concentration of available stock solution. Moreover, due to uncertain LPS molar mass and exact concentration, as well as uncertainty about the number of hydrolysable phosphates, we did not determine the kinetic parameters (K_M and k_{cat}). Likewise, kinetic parameters for 2.5 μM pNPP could not be determined due to low concentration being incompatible with our fitting procedure (See Supplementary Fig. 24). Conditions: 15 nM PEG nanoantenna, 5 nM SA, 10 nM bAP, 2.5 μM pNPP or ~2.5 μM LPS, in 100 mM Tris, 10 mM NaCl, 37 °C, pH 8.0.

The colours in the simplified scheme of LPS represent acyl chains (grey), phosphate (red), ethanolamine (green), *N*-acetylglucosamine (orange), ketodeoxyoctonic acid (yellow), heptose (violet), glucose (dark blue), neutral sugar (brown), colitose (light blue). Note that LPS structure can differ for various strains of bacteria.

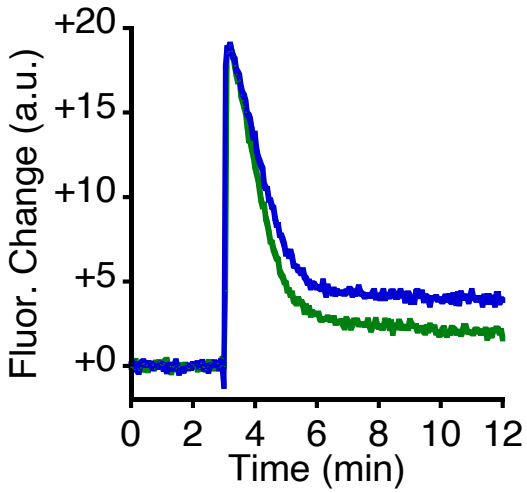

Supplementary Fig. 28. Variation in baseline after substrate hydrolysis. In Fig. 3, the baseline after the reaction can differ between substrates. However, we observed a similar result for different trials of the same substrate. For example, two trials of 4MUP hydrolysis from are shown here. In both cases, the signal increase (~19 a.u.) and reaction completion time (~6 min) are essentially the same, but the baselines after the reaction are less reproducible. At present, we do not have an explanation for this effect.

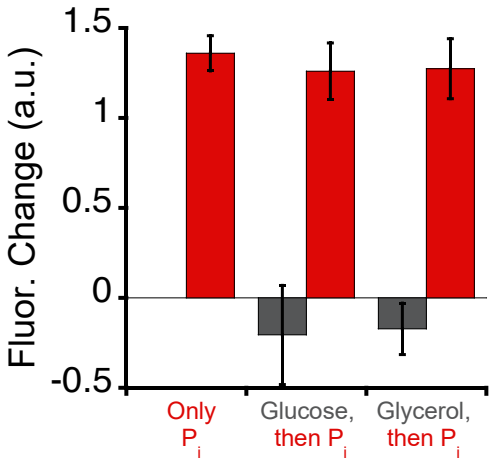

Supplementary Fig. 29. Increase in baseline after the reaction is linked to the presence of phosphate. We further explored the origin of the baseline increase observed following hydrolysis for some substrates in Fig. 3. Here, we explore the effect of adding the product(s) of the reaction to the nanoantenna-SA-bAP complex. We find that only phosphate (P_i) increased the signal baseline, but for example, not the other products of G6P and BGP (glucose and glycerol, respectively). All experiments were performed with n=1 biologically independent enzyme samples examined over 3 independent experiments. Data are presented as mean values ± SEM.

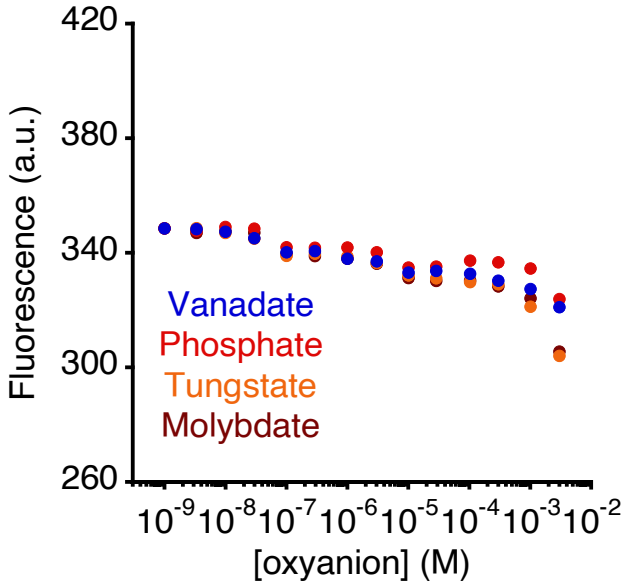

Supplementary Fig. 30. Addition of oxyanions does not affect the fluorescence of the nanoantenna – no bAP. Fluorescence of the L12 ssDNA nanoantenna attached to SA, but without bAP, was not substantially affected by the addition of vanadate, phosphate, tungstate or molybdate.

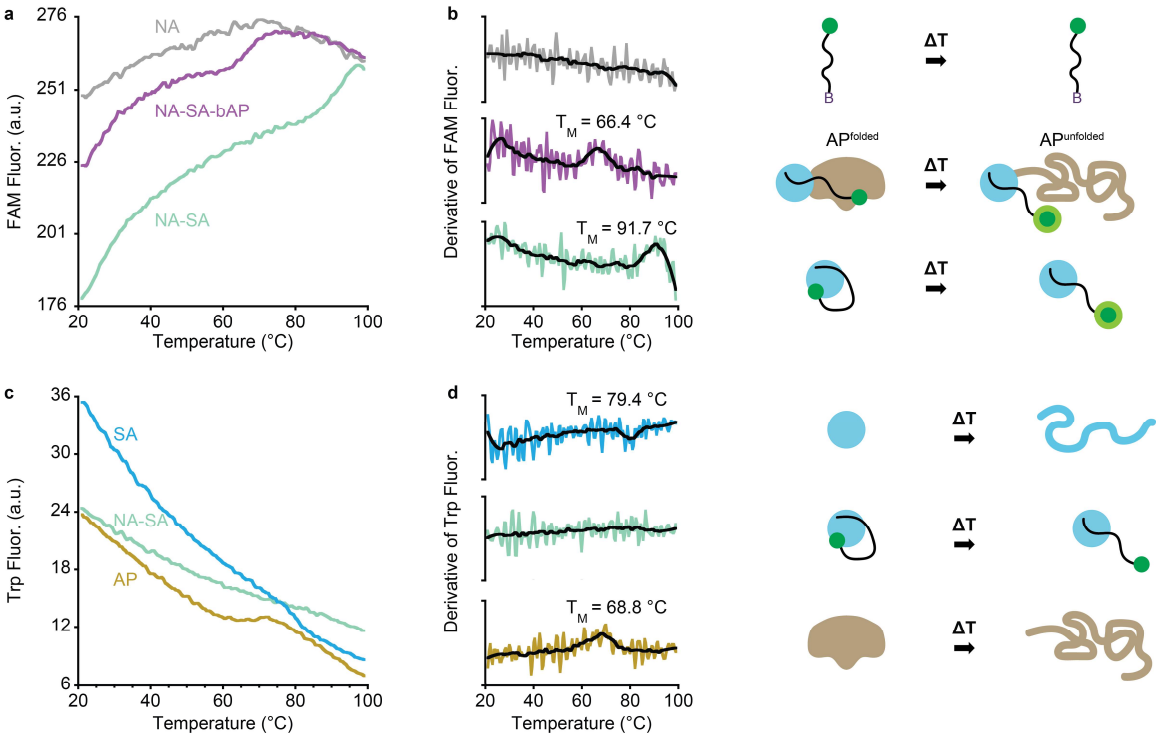

Supplementary Fig. 31. Monitoring protein unfolding with fluorescent nanoantennas. (a) FAM fluorescence melting curves of the nanoantenna (grey), nanoantenna-SA platform (green) and nanoantenna-SA-bAP complex (purple). (b) Derivatives of the melting curves with smoothing (black lines) and corresponding cartoons are shown. (c) Trp fluorescence melting curves of SA (blue), the nanoantenna-SA platform (green) and AP (dark yellow). (d) Derivatives of the melting curves with smoothing and corresponding cartoons are similarly shown. Note that we did not record melting curves of bAP alone by Trp fluorescence due to the high concentration of BSA stabilizer added by the manufacturer. Conditions: 150 nM nanoantenna, 50 nM SA, 100 nM bAP in 100 mM NaCl, 50 mM Na_2HPO_4, pH 6.99, 20-100 °C, 1 °C/min. $\lambda_{ex}/_{em}$ FAM = 498/520 nm, Trp = 280/340 nm. Smoothing of the derivatives was by the Savitzky–Golay method with 25 points.

First, we consider the nanoantenna and SA. Using FAM fluorescence, we see that the nanoantenna alone does not display a transition. Using Trp fluorescence, we see that SA alone displays a transition at 79.4 °C ± 1.0 °C. This indicates the melting temperature (T_M) of SA and it agrees with the reported literature value.[52, 53]

Next, we consider the nanoantenna-SA platform. Using Trp fluorescence, we see that it does not display a transition. This is due to the enhanced cooperativity of the thermal unfolding of SA upon biotin binding.[52] Thus, the nanoantenna-SA platform remains stable over the tested temperature range. Using FAM fluorescence, however, the nanoantenna-SA platform displays a transition at 91.7 °C ± 0.7 °C. We attribute this to the dissociation of the FAM component of the nanoantenna from the surface of SA.

Finally, we consider AP and the nanoantenna-SA-bAP complex. Using Trp fluorescence of AP, we observe a transition at 68.8 °C ± 0.4 °C, which agrees with the reported literature value for AP melting temperature (T_M).[54, 55] Using FAM fluorescence of the nanoantenna-SA-bAP complex, we observe the same transition at 66.4 °C ± 0.1 °C. Notably, the signal with FAM fluorescence is ~10x stronger than with Trp fluorescence, and it can avoid the fluorescence background arising from other proteins (*e.g.*, BSA).

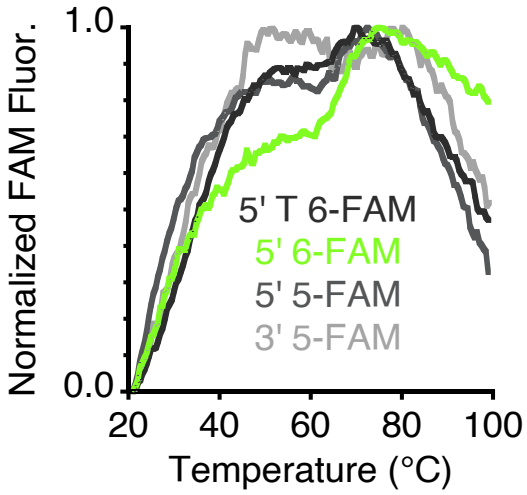

Supplementary Fig. 32. Different FAM connections affect the sensitivity of the nanoantenna towards detecting the melting transition. The L12 nanoantenna with 5′ 6-FAM is more efficient to detect bAP melting compared to analogous nanoantennas with 5′ T 6-FAM, 5′ 5-FAM or 3′ 5-FAM. See Extended Data Fig. 6 for the types of FAM.[56]

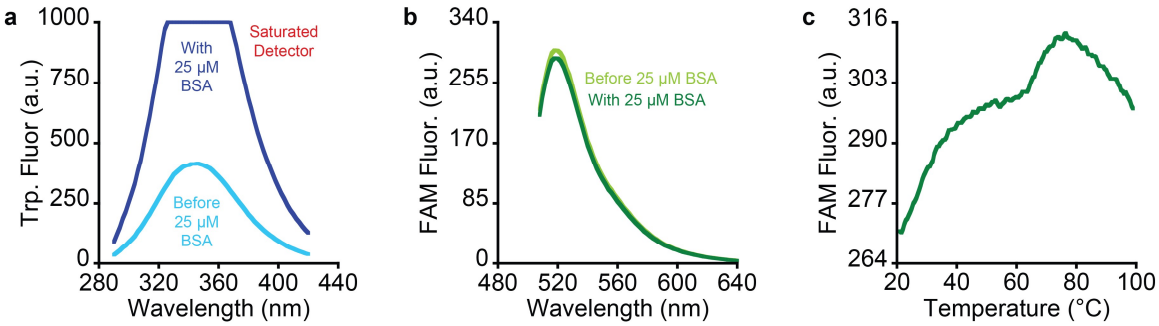

Supplementary Fig. 33. Monitoring unfolding transition of proteins using nanoantenna in a complex sample. (a) Adding BSA to the cuvette results in a tryptophan fluorescence signal that saturates the detector. This reduces the usefulness of tryptophan to monitor unfolding transition in complex environment. (b) The same condition does not affect the FAM fluorescence, (c) thereby still allowing specific monitoring of the bAP thermal unfolding transition.

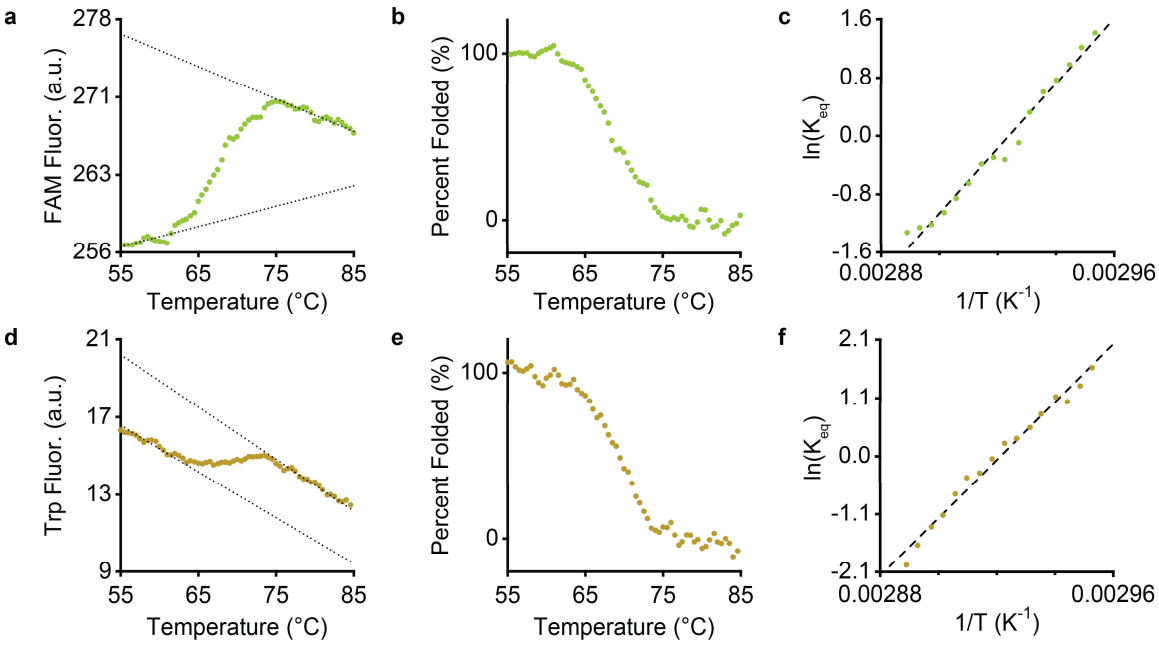

Supplementary Fig. 34. Determination of the apparent Gibbs free energy (Δ*G*) of bAP. (a) Example fitting of the melting curve of the nanoantenna-SA-bAP complex with linear regression to normalize the fluorescence data. (b) The normalized data shows the percent of folded and unfolded conformation. (c) Van't Hoff plot of the data allows one to determine the apparent Δ*G* for the unfolding of bAP. Using the nanoantenna strategy (FAM fluorescence), we determined an apparent Δ*G* of -7.8 ± 0.5 kcal/mol. (d-f) Using the more conventional Trp fluorescence on AP alone, we find a similar value of -9.1 ± 0.3 kcal/mol. All experiments were performed with n=1 biologically independent enzyme samples examined over 3 independent experiments. Data are presented as mean values ± SEM.

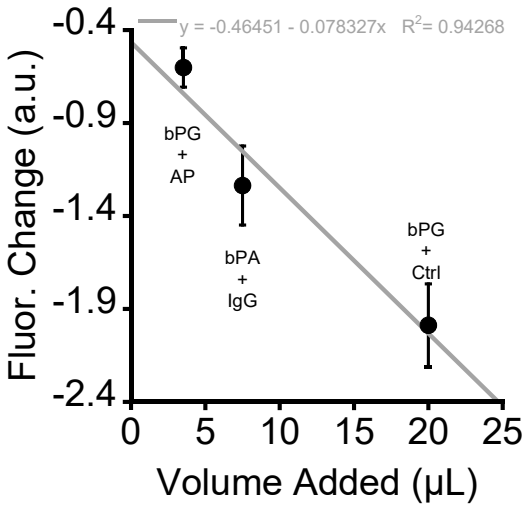

Supplementary Fig. 35. Effect of dilution in control experiments. The signal decrease in the controls in Fig. 6f correlates with the volume of sample added (3.52 µL AP, 7.5 µL goat IgG, 20 µL SARS-CoV-2 antibodies ctrl). All experiments were performed with n=1 biologically independent enzyme samples examined over 3 independent experiments. Data are presented as mean values ± SEM.

Supplementary Table 1. Michaelis–Menten kinetic parameters of AP with pNPP substrate reported in the literature[45] and values determined in our study. Our fitting strategy of the nanoantenna fluorescence shown in Fig. 2d-e displays similar parameters. Control UV–Vis experiments shown in Supplementary Fig. 22 also display similar parameters.

	Literature ITC	**Literature** UV-Vis	**Nanoantenna** Fluorescence (Fig. 2d-e)	**Nanoantenna** UV–Vis (Fig. S22a)	**Dummy** UV–Vis (Fig. S22b)	**bAP Only** UV–Vis (Fig. S22c)
K_M **(μM)**	7.78	9.31	5.0 ± 0.1	10.1 ± 0.7	11.3 ± 1.0	7.9 ± 0.2
V_{max} **(μM s^{-1})**	n/a	n/a	0.321 ± 0.0(8)[b]	2.7 ± 0.0(1)	3.3 ± 0.0(5)	3.2 ± 0.0(1)
k_{cat} **(s^{-1})**	47.36	46.92	32.1 ± 0.8	24.6 ± 0.0(48)	30.4 ± 0.4	30.0 ± 0.1
k_{cat}/K_M **(μM^{-1} s^{-1})**	6.1[a]	5.0[a]	6.4 ± 0.3	2.5 ± 0.2	2.7 ± 0.2	3.8 ± 0.1

a) These k_{cat}/K_M values differ slightly from what was reported in Table 1 of the cited study,[45] because the reported k_{cat}/K_M values seemingly do not agree with the corresponding k_{cat} and K_M values, so we recalculated it. The differences are small, and in practical terms, do not matter.

b) This V_{max} was derived by using the k_{cat} value obtained from our fitting procedure and enzyme concentration, rather than the standard way of deriving the k_{cat} from the V_{max} and enzyme concentration. Note also that the fluorescence experiment used 10 nM bAP, and the UV–Vis experiments used 109 nM bAP, hence the differing V_{max} values. As expected, the k_{cat} values were effectively the same.

Supplementary Table 2. Determined K_i values for phosphate. Conditions: 100 mM Tris, 10 mM NaCl, pH 8.0, 30 °C, pNPP substrate. Also shown are literature values determined under similar conditions.

Inhibitor	This Study	Literature				
	K_i (μM)	K_i (μM)	pH	Temp (°C)	Substrate	ref
P_i or PO_4^{3-} *phosphate*	48.4 ± 2.0	16.5	9.25	30	4MUP	[57]
		19	9.25	30	ATP	[57]
		21.2	7.5	37	PP_i	[58]
		29	9.19	30	PP_i	[57]
		33.7	7.0	25	ATP	[45]
		60	8.9	37	PLP	[59, 60]
		68	9.25	30	fluorophosphate	[57]
		130[a]	9.0	30	pNPP	[61]

a) Human intestine was used in this study.

Supplementary Table 3. Determined K_M and k_{cat} values for various substrates (Fig. 3). Also shown are literature values, listed from low to high K_M, that were determined under similar conditions.[a,b] Our k_{cat} and K_M values determined at pH 8.0 and 37 °C are within the typical range for AP values (see pNPP), but are obviously faster when compared to most available values for other substrates determined at somewhat lower pH or temperature.

	Substrate	This Study			Literature					
		k_{cat} (s^{-1})	K_M (μM)	k_{cat}/K_M ($\mu M^{-1}\ s^{-1}$)	k_{cat} (s^{-1})	K_M (μM)	k_{cat}/K_M ($\mu M^{-1}\ s^{-1}$)	pH	T (°C)	ref
Assay molecules	**pNPP** *p-nitrophenylphosphate*	178.1 ± 12.8	24.3 ± 1.3	7.3 ± 0.9	-	3.6	-	8.0	25	62
					47.36	7.78	6.1[c]	8.0	30	45
					46.92	9.31	5.0[c]	8.0	30	45
					300.3	10.7	28.1	8.0	25	63
					287	18	16.0	8.0	RT	64
					22.5	24	0.93	7.4	25	65
					3580	35	99	8.5	25	66
					905	37.7	24.0	8.0	37	67
					-	~63[d]	-	8.0	-	32
					341.7	119.7	2.9	8.8	37	68
	4MUP *4-methylumbelliferyl phosphate*	237.6 ± 12.9	20.5 ± 0.6	11.6 ± 1.0	39.2	2.2	18	8.0	25	69
					-	2.3[e]	-	7.91	30	70
					9.5	2.5	3.8[c]	8.0	25	45
					7.2	3.2	2.6[c]	8.0	25	45
					-	5.4[e]	-	8.36	30	70
					-	~10	-	8.5	22	71
					-	28	-	8.5	30	72
Biomolecules	**PP_i** *pyrophosphate*	242.5 ± 16.7	17.3 ± 0.2	14.0 ± 1.1	-	16	-	8.0	25	62
					36.6[f]	66[f]	0.55[f]	7.4	25	65
	BGP *β-glycerophosphate*	224.1 ± 14.1	48.2 ± 2.8	4.6 ± 0.6	-	15	-	8.0	25	62
	PEP *phosphoenolpyruvate*	296.5 ± 12.3	13.1 ± 0.2	22.6 ± 1.3	-	5.5	-	8.0	25	62
	PSer *phosphoserine*[f]	162.2 ± 5.2	48.4 ± 1.0	3.4 ± 0.2	-	-	-	-	-	-
	PLP *pyridoxal-5'-phosphate*	157.2 ± 12.5	58.9 ± 11.6	2.7 ± 0.7	-	3.6	-	7.4	37	73
					17.8	31	0.57	7.4	25	65
	G6P *glucose-6-phosphate*[f]	114.5 ± 11.8	75.8 ± 14.3	1.5 ± 0.4	-	-	-	-	-	-
	F6P *fructose-6-phosphate*[f]	106.8 ± 3.2	98.5 ± 16.0	1.1 ± 0.2	-	-	-	-	-	-
	AMP *adenosine monophosphate*	168.3 ± 12.4	43.5 ± 2.4	3.9 ± 0.5	-	11.2	-	8.0	30	74
					-	12.0	-	7.4	30	74
					-	18	-	8.0	25	62
					22.6	43	0.52	7.4	25	65
	ADP *adenosine diphosphate*	216.1 ± 14.3	50.0 ± 2.8	4.3 ± 0.5	22.6	20	1.13	7.4	25	65
	ATP *adenosine triphosphate*	144.5 ± 4.0	46.7 ± 2.9	3.1 ± 0.3	3.5	6.8	0.52	7.0	25	45
					-	16	-	8.0	25	62
					-	18.9	-	8.2	25	75
					18.9	31	0.61	7.4	25	65
					-	105	-	7.5	37	76
	GTP *guanosine triphosphate*[f]	218.4 ± 19.6	41.1 ± 1.0	5.3 ± 0.6	-	-	-	-	-	-
	PCr *phosphocreatine*[f]	161.1 ± 6.5	61.0 ± 7.0	2.6 ± 0.4	-	-	-	-	-	-
Drug	**Amifostine** *also called Ethyol*[f]	87.0 ± 2.5	39.1 ± 3.9	2.2 ± 0.3	-	-	-	-	-	-

a) Our conditions were 100 mM Tris, 10 mM NaCl, pH 8.0, 37 °C; also 150 nM nanoantenna, 50 nM SA, 20 nM bAP, 300 μM substrate. Literature conditions were mostly Tris buffers, pH ~8, 25-37 °C. We did not consider studies at significantly different pH, nor with AP from other species/isoforms.

b) $[Mg^{2+}]$ can affect the rate of substrate hydrolysis, so values could differ between studies, but likely not enough to make the results non-comparable. For example, in one study at pH 8.0, 1 mM or 5 mM of Mg^{2+} increased the rate by factors of about ~1.7x or ~2.2x, respectively.[32]

c) See Supplementary Table 1, note a.

d) This literature pNPP K_M value was not reported directly. We estimated it from the Lineweaver-Burk plot in Figure 3 of the cited study.[32]

e) These literature 4MUP K_M values were not reported directly. We determined them by non-linear fitting with the Michaelis-Menten equation in KaleidaGraph of the data found in Table 2 of the cited study.[70]

f) We could not find any studies reporting kinetic parameters for calf intestinal alkaline phosphatase with some substrates under similar conditions. However, there are studies with various biomolecular substrates that we did not consider for comparison because they employed different conditions (*e.g.*, pH 9-11),[57, 77-80] other bovine isoforms (*e.g.*, kidney),[81-84] other mammalian species (*e.g.*, human, pig, rat),[77, 79, 80, 85-98] or APs from very different species (*e.g.*, fish, bacteria, yeast).[78, 99-111, 112]

Supplementary Table 4. Kinetic parameters for amifostine with various effectors determined from the data in Fig. 4. Fitting was done analogously to Fig. 3, and then the apparent K_M was used to determine the K_i. Also shown are the K_d (μM) values determined in Fig. 5.

Effector	k_{cat} (s^{-1})	K_M (μM)	K_i (μM)	K_d (μM)
None	76.0 ± 9.4	43.0 ± 5.6	-	-
PO_4^{3-} *phosphate*	77.6 ± 5.7	85.1 ± 11.6	30.6 ± 8.2	No plateau
MoO_4^{2-} *molybdate*	71.3 ± 6.6	107.0 ± 13.8	20.1 ± 5.2	No plateau
WO_4^{2-} *tungstate*	46.5 ± 9.8 *	170.6 ± 36.5	10.1 ± 3.5	7.6 ± 0.2 (7.55 ± 0.23) **
AsO_4^{3-} *arsenate*	28.6 ± 2.9 *	394.9 ± 52.8	3.7 ± 1.0	Not tested
VO_4^{3-} *vanadate*	25.1 ± 4.0 *	1130.7 ± 119.5	1.2 ± 0.3	0.5 ± 0.0 (0.54 ± 0.01) **
Mg^{2+} *magnesium ion*	116.5 ± 13.9	60.1 ± 8.9	-	Not tested

Overall, our results agreed with previous studies of inhibitor potency for various APs:
vanadate > arsenate > tungstate > molybdate > phosphate (CIAP, pH 8.0, 37 °C, amifostine)

1) vanadate > tungstate > molybdate (*E. coli* AP, pH 8.0, 23 °C, pNPP)[113]
2) vanadate > tungstate > molybdate (sludge-associated AP, pH 8.00, 30 °C, 4MUP)[114]
3) vanadate > tungstate > molybdate (goldfish ovarian tissue AP, 20 °C, pNPP)[115]
4) vanadate > tungstate ≥ arsenate (bovine intestinal mucosa AP, monofluorophosphate)[116]
5) tungstate ≥ arsenate > molybdate (bovine intestinal AP, pH 7.4?, room temp., pNPP)[117]
6) vanadate > arsenate (calf intestinal AP, pH 9.5, 25 and 40 °C, AttoPhos)[118]
7) arsenate > phosphate (calf intestinal AP, pH 9.95, 38 °C, phenyl phosphate)[119]
8) arsenate > phosphate (equine plasma AP, pH 10.3, 30 °C?, phenyl phosphate)[120]
9) vanadate > phosphate (human intestinal AP, pH 9.0, 40 °C, pNPP)[61]
10) vanadate > phosphate (bovine kidney AP, pH 10.0, 30 °C, pNPP)[23]
11) vanadate > arsenate > phosphate (epiphyseal cartilage membrane AP, pH 7.5, 37 °C, pNPP or PP_i)[121]

We also observed that, as expected, Mg^{2+} increased both the k_{cat} and the K_M.[32]

This analysis was performed several months after our values obtained for amifostine in Fig. 3, which further shows the reproducibility of the method.

* k_{cat} should not decrease for a competitive inhibitor, but we did observe this for tungstate, arsenate, and vanadate. However, we found that fitting the nanoantenna spike without the reaction having finished reduces the determined k_{cat} of the reaction. For example, if we fit the phosphate data for 30 min or 20 min, its k_{cat} remains effectively unchanged. However, if we fit the same data using only a 10 min or 5 min time window (*i.e.*, when the reaction is not yet over), then the determined k_{cat} decreases while there was only a small effect on the K_M (data not shown). This potential artifact of the fitting should be kept in mind when screening inhibitors with high potency and long reaction time.

** Usually, we showed the error to one decimal place, but showed it to two decimal places since it was 0.0 for vanadate.

Supplementary Note 1. Discussion of enzymatic reactions.

In (a) and (b) in Extended Data Fig. 1, important studies of the different states of AP are highlighted. The crystal structure enables one to study unbound (AP) and product-bound AP (AP-P_i).[54, 122-127] An approximation of the transition state geometry can be achieved with the help of a transition state analogue (TSA) inhibitor, *e.g.,* vanadate (AP-V_i).[128, 129] To study AP-mediated hydrolysis of a substrate in real-time, typical methods involve monitoring the generation of a colorimetric product from *p*-nitrophenylphosphate (pNPP)[130] or a fluorescent product from 4-methylumbelliferyl phosphate (4MUP)[70] or its analogues.[131] Newer strategies using fluorescence have been developed, including those for monitoring substrate consumption,[132] ratiometric monitoring of substrate consumption and product generation,[133-139] and various others.[140-151] Moreover, other spectroscopic[152-159] and electrochemical[160-165] methods have also been reported. However, while these synthetic substrates are easy to detect by fluorescence and other methods, biomolecular substrates remain spectroscopically silent. Some strategies use released P_i to generate a signal, but this sequestration of P_i could potentially affect the observed kinetics since it is a competitive inhibitor.[166-169] Thus, real-time analysis of biomolecules has been limited to substrate-specific assays, mainly for PP_i,[58, 170-174] and ATP,[75, 76, 175-178] but also other molecules.[73, 179-181] Note that not all of these studies were used to characterize AP kinetics, and some were for the purpose of detecting AP. Some methods can detect phosphopeptides[182] or molecules with a pyrophosphate moiety,[183] but they are still not universal. For most biomolecules, one must instead quantify the phosphate product via a phosphomolybdate complex,[184, 185] or newer strategies,[186] which do not permit real-time analysis. ITC-based initial rate calorimetry (IrCal) has also been reported. It monitors heat released and is label-free,[45, 66] but it suffers from the drawbacks discussed in the Introduction. In contrast, our fluorescent nanoantennas allow real-time monitoring of any substrate via conformational changes occurring between the enzyme and the transient enzyme-substrate complex.

Supplementary Note 2. Notes about nanoantenna selection: from screening to application

We propose the following steps as a guideline to rapidly identify a working nanoantenna for monitoring a specific protein function.

1. Biotinylation of the protein of interest. This step can be readily done, for example, by reacting the protein with a N-hydroxysuccinimide-biotin conjugate (NHS-biotin). Biotinylation kits for this procedure are commercially available, and the synthesis and purification process take roughly one day. Proteins can often be biotinylated without significantly affecting their functions,[46] but the user should not assume this and should make sure that the protein is still functional. Some companies also sell biotinylated proteins. In this work, we have used the convenient biotin-streptavidin system to rapidly screen our nanoantennas, but other attachment strategies could also be employed (*e.g.,* direct nanoantenna attachment to a lysine residue via thiol chemistry, alternatives to streptavidin such as avidin and neutravidin, or other noncovalent platform strategies).

2. Nanoantennas. Biotinylated and fluorophore-labeled DNA- and PEG-based nanoantennas can be synthesized by automated phosphoramidite chemistry. For most users, however, one can purchase labeled oligonucleotides from a commercial nucleic acid supplier. We would also be happy to share a preliminary library of our nanoantennas with future potential users.

3. Screening nanoantennas to detect protein function. In our experience, one can rapidly screen dozens of nanoantennas via the nanoantenna-streptavidin platform to find one that suitably detects protein function. Of course, it is certainly possible to test more! Screening can be done in a 96-well plate but also conveniently works in a simple cuvette setup. Ideally, one would screen nanoantennas of various linker lengths, linker types, and with diverse fluorophores. Here, we describe two types of screening procedures based on whether the protein function involves a transient or stable signal.

3a. For experiments that provide a stable signal (*e.g.*, a protein binding a ligand or an antibody), one can conveniently use the 96-well plate format to screen for which nanoantenna(s) detects the binding event with the largest signal change.

3b. For experiments that provide a transient signal (*e.g.*, an enzymatic reaction), and which may not be amenable to the 96-well plate format due to the dead time and speed of the kinetic event, our experience with bAP has been that nanoantennas that best detect the binding of the biotinylated protein to the nanoantenna-streptavidin platform are also the best to detect its function. Therefore, one could rapidly screen for the nanoantenna that most sensitively detects protein attachment to streptavidin. The winner nanoantennas can then subsequently be tested in cuvettes for their ability to specifically report a conformational change.

There are effectively limitless combinations of nanoantennas containing different fluorophores, linker compositions and lengths, and chemical modifiers. Thus, a second screening round might be of value. For example, a second screening could involve different linker lengths or compositions for a specific working fluorophore. Furthermore, although we noticed that small modifications typically do not render a nanoantenna completely ineffective, these small modifications (*e.g.*, the chemical connection of a fluorophore) can potentially enhance the sensitivity of the nanoantenna (*e.g.,* T 6-FAM vs 5-FAM vs 6-FAM, or a type of FAM at the 5′-end vs the 3′-end). These additional rounds of screening may not be necessary, but could help with tuning the signal, if desired. Alternatively, one could screen a wide array of nanoantennas in a single round.

4. Validate the candidate nanoantennas. After rapidly screening the nanoantennas, one can test the best candidate(s) in cuvettes or any other desired format to find out which one works best for a specific protein function of interest. This includes analysis of conformational change, transient intermediates, binding events, and so on.

List of reagents.

Enzymes and proteins. Alkaline phosphatase (AP) was from calf intestinal mucosa of *Bos taurus*. Unconjugated AP (19.83 mg/ml, in 0.05 M Tris Chloride, 0.005 M $MgCl_2$, 0.0001 M $ZnCl_2$, 50% (v/v) Glycerol, pH 7.0; >6,000 units/mg, where unit = hydrolysis of ~6 mM p-nitrophenolphosphate/ minute at 37°C at pH 9.8), biotin-conjugated AP (bAP; 1 mg/ml, in 0.05 M Tris Chloride, 0.15 M NaCl, 0.001 M $MgCl_2$, 0.0001 M $ZnCl_2$, 50% (v/v) Glycerol; pH 8.0, 0.05% (w/v) Sodium Azide as a preservative, 10 mg/mL Bovine Serum Albumin (BSA) as a stabilizer), streptavidin-conjugated AP (SA-AP; 1 mg/ml, in same buffer from manufacturer), biotin-conjugated glucose oxidase (bGOx; 0.01 M Sodium Phosphate, 0.15 M Sodium Chloride, pH 7.2), Protein G Biotin Conjugated (bPG; lyophilized, 1.0 mg/ml, 0.02 M Potassium Phosphate, 0.15 M Sodium Chloride, pH 7.2, 0.01% (w/v) Sodium Azide as a preservative, 10 mg/mL Bovine Serum Albumin (BSA) as a stabilizer), Protein A Biotin Conjugated (bPA; lyophilized, 1.0 mg/mL, 0.02 M Potassium Phosphate, 0.15 M Sodium Chloride, pH 7.2, 0.01% (w/v) Sodium Azide as a preservative, 10 mg/mL Bovine Serum Albumin (BSA) as a stabilizer), and Goat IgG whole molecule (lyophilized, 11.0 mg/ml, 0.02 M Potassium Phosphate, 0.15 M Sodium Chloride, pH 7.2, 0.01% (w/v) Sodium Azide as a preservative, lot # 32090) were from Rockland Immunochemicals (Limerick, PA, USA). Streptavidin from *Streptomyces avidinii* (SA; 1 mg/ml, in 140 mM NaCl, 8 mM Sodium Phosphate, 2 mM potassium phosphate, 10 mM KCl, pH 7.4) was from New England Biolabs (Ipswich, MA, USA). VIROTROL SARS-CoV-2 (Reactive for SARS-CoV-2 total IgG/IgM and IgG antibodies; human plasma based; lot # 390300) and VIROCLEAR SARS-CoV-2 (Non-reactive for SARS-CoV-2 total IgG/IgM and IgG antibodies; human plasma based; lot # 390600) were from Bio-Rad Laboratories (Hercules, CA, USA). Bovine Serum Albumin (BSA; cold ethanol fraction, pH 5.2, ≥96%) was from Sigma-Aldrich (St. Louis, MO, USA).

Substrates and inhibitors. *p*-nitrophenylphosphate (pNPP, 500 mM solution) was from New England Biolabs. Adenosine 5′-triphosphate (ATP; 100 mM solution, pH 7.0) was from Bio Basic (Markham, ON, Canada). Pyridoxal-5'-phosphate monohydrate (PLP; ≥95%) and creatine phosphate disodium tetrahydrate (PCr; ≥98%) were from BioShop (Burlington, ON, Canada). Amifostine (≥98%) was from BioVision (Milpitas, CA, USA). 4-Methylumbelliferyl phosphate (4MUP; ≥98%), sodium pyrophosphate tetrabasic decahydrate (PP_i; ≥99%), β-glycerophosphate disodium salt hydrate (BGP; “cell culture tested”), phospho(enol)pyruvic acid monopotassium salt (PEP; 99%), O-phospho-L-serine (PSer; ≥98%), D-glucose 6-phosphate sodium salt (G6P; ≥98%), D-fructose 6-phosphate disodium salt (F6P; ≥98%), adenosine 5′-monophosphate monohydrate (AMP; ≥95%), adenosine 5′-diphosphate sodium salt (ADP; ≥95%), guanosine 5′-triphosphate sodium salt hydrate (GTP; ≥95%), 4-nitrophenol (PNP; spectroscopic grade), sodium orthovanadate (99.98%), sodium molybdate dihydrate (≥99%), potassium arsenate monobasic (≥99.9%), α-D-glucose (anhydrous, 96%), were from Sigma-Aldrich. Lipopolysaccharide (LPS) solution from *Escherichia coli* O26:B6 (eBioscience, “sterile aqueous buffer, no sodium azide”) was from Thermo Fisher Scientific (Waltham, MA, USA). Sodium tungstate dihydrate was from MCB (Norwood, OH, USA). Glycerol (99.5%) was from American Chemicals.

Oligonucleotide synthesis reagents. 3′-modifications were from controlled pore glass (CPG) columns and 5′-modifications were from phosphoramidites. Biotin (B), Quasar 570 (Q570), Quasar 670 (Q670), fluorescein (5-FAM), rhodamine-X (ROX), CAL Fluor Orange 560 (CAL), phosphate (P), C16 spacer (C16), thiol C6 (S-S; S-H after treatment with dithiothreitol) CPG columns, as well as Fluorescein T Amidite (T 6-FAM or T_{FAM}), 6-FAM Amidite (6-FAM), 5-FAM Amidite (5-FAM), Biotin T C6 Amidite (T_B), Spacer 18 Amidite (DMT-Hexa(ethylene glycol)) (S18), and Methylene Blue Succinimidyl Ester (MB) were from Biosearch Technologies (Petaluma, CA, USA). Tetramethylrhodamine (TAMRA) and Cyanine 3 (Cy3) CPG columns were from Glen Research (Stirling, VA, USA). Standard A, G, C, T CPG columns were from Biosearch Technologies. Acetonitrile (wash grade), DMT removal (3% trichloroacetic acid/dichloromethane), CAP A (Acetic Anhydride/Pyridine/THF), CAP B (16% N-Methylimidazole in THF), Oxidation Solution (0.1M Iodine/Pyridine/H_2O/THF), Activation Reagent (0.25 M 5-ethylthio Tetrazole in ACN), deoxycytadine (n-acetyl) CED phosphoramidite, deoxyguanosine (n-ibu) CED phosphoramidite, deoxyadenosine (n-bz) CED phosphoramidite and thymidine CED phosphoramidite were from

ChemGenes (Wilmington, MA, USA). For purification, glacial acetic acid (99.7%) and triethylamine (99%) were from Thermo Fisher Scientific, acetonitrile (≥99.9) was from Sigma-Aldrich, and trifluoroacetic acid (99%) was from Alfa Aesar (Ward Hill, MA, USA). MicroPure II columns for DNA purification were from Biosearch.

Buffers and miscellaneous. Biotin (5-fluorecein) conjugate (≥90%) used as the L0 nanoantenna was from Sigma-Aldrich, 8-Anilino-1-naphthalenesulfonic acid ammonium salt hydrate (ANS probe; 97%), CAPS (≥99%), MOPS sodium salt (≥99.5%), Bis-Tris (≥98.0%) and hydrochloric acid (37%) were from Sigma-Aldrich. D-Biotin (99.0%), Tris (99.9%), sodium chloride (≥99.5%), sodium hydroxide (98%), PIPES (99%) and sodium phosphate dibasic were from BioShop. Magnesium chloride anhydrous (99%) was from Alfa Aesar. Sodium phosphate monobasic anhydrous (≥99.5%) and ammonium hydroxide (28-30%) were from VWR (Radnor, PA, USA). HEPES was from MP Biomedicals (Solon, OH, USA). All reagents were stored at -20°C, -4 °C or at room temperature, as appropriate. All solutions were prepared in ultrapure water from a Milli-Q Biocel filtration device from EMD Millipore (Burlington, MA, USA).

List of oligonucleotides sequences.
All sequences listed here are in the direction of 5′ to 3′.

PEG nanoantennas:
~L21: T_{FAM}-S18-S18-S18-Biotin (S18 = Spacer 18)
~L41: T_{FAM}-S18-S18-S18-S18-S18-S18-Biotin
Note that length is estimated in Supplementary Fig. 2.

ssDNA nanoantennas with $T_{6\text{-}FAM}$:
L6: $T_{6\text{-}FAM}$-TATTG-Biotin
L12: $T_{6\text{-}FAM}$-TATTGATCGGC-Biotin
L24: $T_{6\text{-}FAM}$-TATTGATCGGCGTTTTAAAGTG T-Biotin
L48: $T_{6\text{-}FAM}$-TATTGATCGGCGTTTTAAAGTGTCCAGGGTGTTTGTGTATTACTCGA-Biotin
PolyT12: $T_{6\text{-}FAM}$-TTTTTTTTTT-Biotin

ssDNA nanoantennas with other FAMs:
L12 (6-FAM version): 6-FAM-TTATTGATCGGC-Biotin
L12 (5-FAM version): 5-FAM-TTATTGATCGGC-Biotin

Note that 5-FAM and 6-FAM are isomers (see Extended Data Fig. 6). Therefore, the nanoantennas L12, L12 (6-FAM version), and L12 (5-FAM version) differ in their connection of FAM at the 5′-end. In addition, we also used rL12 (5-FAM), see below, which had the dye at the 3′-end.

cDNA to form dsDNA nanoantennas:
cL12: GCCGATCAATAA
cL24: ACACTTTAAAACGCCGATCAATAA
cL48: TCGAGTAATACACAAACACCCTGGACACTTTAAAACGCCGATCAATAA

L12 with other dyes:
To test various dyes, we used a “reverse” version of the L12 nanoantenna (rL12).
rL12 (Dye): T_{Biotin}-TATTGATCGGC-Dye; where dye = 5-FAM, TAMRA, Cy3, Q570, or Q670
Some dyes were directly attached to a nucleobase, so the sequence was modified accordingly.
rL12 (Dye): T_{Biotin}-TATTGATCGG-C_{Dye}; Dye = ROX or P650
rL12 (Dye): T_{Biotin}-TATTGATCGG-T_{Dye}; Dye = CAL
Thus, for dsDNA with CAL, the cL12’s G at 5′ was replaced by A.
The MB strand was from another project in our lab and was kindly donated by Guichi Zhu.
MB-CCAGAGACCACGGACT-Biotin

Modifiers:
To test chemical modifications near FAM, we used cL12 strand with the Modifier at the 3′-end. Here, Modifier = phosphate, C16, S-S or S-H.
GCCGATCAATAA-Modifier

Dye competition:
For double-dye studies, we used the standard L12 FAM nanoantenna with versions of the cL12 nanoantenna containing CAL, Cy3 or Q670 at the 3′-end. We also used a capture strand analogous to L12 but without the $T_{6\text{-}FAM}$.

Controls:
Molecular beacon: *$T_{6\text{-}FAM}$CCGC*GATCGGCGTTTTA*GCGGA*TCCTGGGTGTTAG-Biotin
Global: $T_{6\text{-}FAM}$-TTTTTTTTTT (Extended Data Fig. 4d)
Dummy: TTTTTTTTTTT-Biotin (Extended Data Fig. 4d)

For nanoantenna-AP covalent attachment, the strand had a thiol moiety. Also, it did not have guanine to avoid side reactions. $T_{6\text{-}FAM}$-CCATACATCCC-SH

Script for fitting kinetic data in MATLAB

1) Model function. This function contains the differential equations of the Michaelis-Menten enzymatic kinetics.

```
function [Tim,ES2] = Model(Eo,Csub,tdil,kcat,Km,Fmax,Fprod)
%Open the Data. Here the data was named Conc100uM1.
load('Conc100uM1')
tdata=Conc100uM1(:,1);
ydata=Conc100uM1(:,2);
%Initial values and time definition
dt = 0.1; %Intervals of 0.1 sec
time = 0:dt:300; %300sec = time of the reaction. Need to be adjusted to the data.
Etot(1,1) = Eo;
S(1,1) = 0;
P(1,1) = 0;
T(1,1) = 0;
ES(1,1) = 0;
%Calculate the Baseline, average of the fluorescence for the first 60 sec (< 63 sec).
ooo = 1:(length(tdata));
logic = tdata(ooo) < 63;
L=length(nonzeros(logic));
Baseline = mean(ydata(1:L));
%We found that it takes about 2 s (tdil) for the substrate to dilute evenly inside the cuvette.
Ratedil=1./tdil;
%Loop calculation of the Michaelis-Menten differential equation.
for o = 1:(length(time)-1)
   if o*dt <= tdil
      RI = Ratedil;
   else
      RI = 0;
   end
   %Rate
   dSdt(o,1) = -Eo.*((kcat.*S(o,1)))./(Km*(1+P(o,1)./48.38) + S(o,1)) + RI.*Csub;
   S(o+1,1) = dSdt(o,1).*dt + S(o,1);
   dPdt(o,1) = Eo.*((kcat.*S(o,1)))./(Km*(1+P(o,1)./48.38) + S(o,1));
   P(o+1,1) = dPdt(o,1).*dt + P(o,1);
   ES(o,1) = Eo.*S(o,1)./(Km*(1+P(o,1)./48.38) + S(o,1));
   Tim(o,1) = time(1,o);
   Prod = P(2:end);
end
% Transforming the ES curve from the Michaelis-Menten into a fluorescence signal.
% From 0 to 60 sec Fluo = Baseline
% From 60 sec to the end Fluo = Baseline + Fmax * [ES] + [P]*Fprod where Fmax is the maximal
fluorescent of the nanoantenna when bound to the ES complex, and Fprod is the fluorescence
impact of the product on the nanoantenna
for oo = 1:(length(Tim))
logic2 = Tim <= 63;
L2=length(nonzeros(logic2));
   if Tim(oo) <= 63
      ES2(oo) = Baseline;
   else
      ES2(oo) = Baseline+Fmax.*ES(oo-L2)+Prod(oo-L2).*Fprod;
   end
end
```

2) tofit function. This function calculates the Michaelis-Menten curves for specific values of k_{cat}, K_M, F_{max} and F_{prod} defined by the vector k.

```
function ypred = tofit(k,tdata)
Eo=0.1;% The concentration of enzyme in µM.
tdil=2;% The dilution time of the substrate in s.
Csub=100;% Concentration of substrate in µM.
kcat=k(1); % kcat.
Km=k(2); % KM.
Fmax=k(3); % Maximal fluorescence of the spike.
Fprod=k(4);% Fluorescence impact of the product in a.u./µM.
[t,y] = Model(Eo,Csub,tdil,kcat,Km,Fmax,Fprod);
%% find predicted values y(tdata)
ypred = interp1(t,y,tdata);
end
```

3) Workplace. Using the tofit function, this script performs a nonlinear curve-fitting to find the best values for k_{cat}, K_M, F_{max} and F_{prod}.

```
%% Loading Data
load('Conc100uM1')
tdata=Conc100uM1(:,1); % x-axis data
ydata=Conc100uM1(:,2); % y-axis data
%% Solve nonlinear curve-fitting (data-fitting) problems in least-squares sense
lb = [1;0.1;200;-1];  %lower boundaries
ub = [100;100;500;1]; %upper boundaries
x0=0.5*[ub-lb]+lb;    %initial point (mid-point of boundaries)
% Nonlinear curve-fitting using the function lsqcurvefit
[x,resnorm,residual,exitflag,output,lambda,jacobian]=lsqcurvefit(@tofit,x0,tdata,ydata,lb,ub,optims
et('Display','off'));
% Calculate the 95% confidence interval using the function nlparci
conf=nlparci(x,residual,'jacobian',jacobian,'alpha',0.05);
CI_low=conf(:,1); % Extract the CI lower limit
CI_upp=conf(:,2); % Extract the CI upper limit
Value=x; % Fittted value
CI=(CI_upp-CI_low)/2; % 95% confidence interval
%Create a vector containing all values and CIs.
Results=[Value(1),CI(1),Value(2),CI(2),Value(3),CI(3),Value(4),CI(4)]
```

Supplementary References

1. Perri, M.J. & Weber, S.H. Web-Based Job Submission Interface for the GAMESS Computational Chemistry Program. *J. Chem. Educ.* **91**, 2206-2208 (2014).
2. Schmidt, M.W. et al. General atomic and molecular electronic structure system. *J. Comput. Chem.* **14**, 1347-1363 (1993).
3. Barca, G.M.J. et al. Recent developments in the general atomic and molecular electronic structure system. *J. Chem. Phys.* **152**, 154102 (2020).
4. Hanson, R.M., Prilusky, J., Renjian, Z., Nakane, T. & Sussman, J.L. JSmol and the Next-Generation Web-Based Representation of 3D Molecular Structure as Applied to Proteopedia. *Isr. J. Chem.* **53**, 207-216 (2013).
5. Becke, A.D. Density-functional thermochemistry. III. The role of exact exchange. *J. Chem. Phys.* **98**, 5648-5652 (1993).
6. Lee, C., Yang, W. & Parr, R.G. Development of the Colle-Salvetti correlation-energy formula into a functional of the electron density. *Phys. Rev. B* **37**, 785-789 (1988).
7. Vosko, S.H., Wilk, L. & Nusair, M. Accurate spin-dependent electron liquid correlation energies for local spin density calculations: a critical analysis. *Can. J. Phys.* **58**, 1200-1211 (1980).
8. Stephens, P.J., Devlin, F.J., Chabalowski, C.F. & Frisch, M.J. Ab Initio Calculation of Vibrational Absorption and Circular Dichroism Spectra Using Density Functional Force Fields. *J. Phys. Chem.* **98**, 11623-11627 (1994).
9. Krishnan, R., Binkley, J.S., Seeger, R. & Pople, J.A. Self-consistent molecular orbital methods. XX. A basis set for correlated wave functions. *J. Chem. Phys.* **72**, 650-654 (1980).
10. McLean, A.D. & Chandler, G.S. Contracted Gaussian basis sets for molecular calculations. I. Second row atoms, Z=11–18. *J. Chem. Phys.* **72**, 5639-5648 (1980).
11. Francl, M.M. et al. Self-consistent molecular orbital methods. XXIII. A polarization-type basis set for second-row elements. *J. Chem. Phys.* **77**, 3654-3665 (1982).
12. Clark, T., Chandrasekhar, J., Spitznagel, G.W. & Schleyer, P.V.R. Efficient diffuse function-augmented basis sets for anion calculations. III. The 3-21+G basis set for first-row elements, Li–F. *J. Comput. Chem.* **4**, 294-301 (1983).
13. Spitznagel, G.W., Clark, T., von Ragué Schleyer, P. & Hehre, W.J. An evaluation of the performance of diffuse function-augmented basis sets for second row elements, Na-Cl. *J. Comput. Chem.* **8**, 1109-1116 (1987).
14. Watson, J.D. & Crick, F.H. Molecular structure of nucleic acids. *Nature* **171**, 737-738 (1953).
15. Roth, E., Glick Azaria, A., Girshevitz, O., Bitler, A. & Garini, Y. Measuring the Conformation and Persistence Length of Single-Stranded DNA Using a DNA Origami Structure. *Nano Lett.* **18**, 6703-6709 (2018).
16. Laitinen, O.H., Hytönen, V.P., Nordlund, H.R. & Kulomaa, M.S. Genetically engineered avidins and streptavidins. *Cell. Mol. Life Sci.* **63**, 2992-3017 (2006).
17. Aslan, F.M., Yu, Y., Vajda, S., Mohr, S.C. & Cantor, C.R. Engineering a novel, stable dimeric streptavidin with lower isoelectric point. *J. Biotechnol.* **128**, 213-225 (2007).
18. Vega-Warner, A.V., Wang, C.-H., Smith, D.M. & Ustunol, Z. Milk Alkaline Phosphatase Purification and Production of Polyclonal Antibodies. *J. Food Sci.* **64**, 601-605 (1999).
19. Chuang, N.-N. & Yang, B.-C. A comparative study of alkaline phosphatases among human placenta, bovine milk, hepatopancreases of shrimp Penaeus monodon (Crustacea: Decapoda) and clam Meretrix lusoria (Bivalvia: Veneidae): To obtain an alkaline phosphatase with improved characteristics as a reporter. *Comp. Biochem. Physiol. B* **96**, 787-789 (1990).
20. Martin, M.M. & Lindqvist, L. The pH dependence of fluorescein fluorescence. *J. Lumin.* **10**, 381-390 (1975).

21. Neish, C.S., Martin, I.L., Henderson, R.M. & Edwardson, J.M. Direct visualization of ligand-protein interactions using atomic force microscopy. *Br. J. Pharmacol.* **135**, 1943-1950 (2002).
22. Weissig, H., Schildge, A., Hoylaerts, M.F., Iqbal, M. & Millán, J.L. Cloning and expression of the bovine intestinal alkaline phosphatase gene: biochemical characterization of the recombinant enzyme. *Biochem. J.* **290**, 503-508 (1993).
23. Mordente, A. et al. Mixed function oxidation and enzymes: Kinetic and structural properties of an oxidatively modified alkaline phosphatase. *Arch. Biochem. Biophys.* **264**, 502-509 (1988).
24. Hung, H.-C. & Chang, G.-G. Multiple unfolding intermediates of human placental alkaline phosphatase in equilibrium urea denaturation. *Biophys. J.* **81**, 3456-3471 (2001).
25. Ásgeirsson, B. & Guðjónsdóttir, K. Reversible inactivation of alkaline phosphatase from Atlantic cod (Gadus morhua) in urea. *Biochim. Biophys. Acta Proteins Proteom.* **1764**, 190-198 (2006).
26. Wang, Z.-J., Ma, W., Yang, J.-M., Kang, Y. & Park, Y.-D. Effects of Cu2+ on alkaline phosphatase from Macrobrachium rosenbergii. *Int. J. Biol. Macromol.* **117**, 116-123 (2018).
27. Abdolrazghi, Z. & Butterworth, P.J. Interaction of Calf Intestinal Alkaline Phosphatase with 8-Anilinonaphthalene-1-Sulphonate. *Enzyme* **30**, 129-133 (1983).
28. Deetanya, P. et al. Interaction of 8-anilinonaphthalene-1-sulfonate with SARS-CoV-2 main protease and its application as a fluorescent probe for inhibitor identification. *Comput. Struct. Biotechnol. J.* **19**, 3364-3371 (2021).
29. Martinez-Gonzalez, A.I., Díaz-Sánchez, Á.G., de la Rosa, L.A., Bustos-Jaimes, I. & Alvarez-Parrilla, E. Inhibition of α-amylase by flavonoids: Structure activity relationship (SAR). *Spectrochim. Acta A* **206**, 437-447 (2019).
30. Thompson, W. & Yielding, K.L. 8-Anilino naphthalene sulfonate binding as a probe for conformational changes induced in glutamate dehydrogenase by regulatory reagents. *Arch. Biochem. Biophys.* **126**, 399-406 (1968).
31. Deshpande, M. & Sathe, S.K. Interactions with 8-Anilinonaphthalene-1-sulfonic Acid (ANS) and Surface Hydrophobicity of Black Gram (Vigna mungo) Phaseolin. *J. Food Sci.* **83**, 1847-1855 (2018).
32. Dean, R.L. Kinetic studies with alkaline phosphatase in the presence and absence of inhibitors and divalent cations. *Biochem. Mol. Biol. Educ.* **30**, 401-407 (2002).
33. Basu, S., Finke, A., Vera, L., Wang, M. & Olieric, V. Making routine native SAD a reality: lessons from beamline X06DA at the Swiss Light Source. *Acta Crystallogr. D* **75**, 262-271 (2019).
34. Fairhead, M., Krndija, D., Lowe, E.D. & Howarth, M. Plug-and-Play Pairing via Defined Divalent Streptavidins. *J. Mol. Biol.* **426**, 199-214 (2014).
35. Kada, G., Falk, H. & Gruber, H.J. Accurate measurement of avidin and streptavidin in crude biofluids with a new, optimized biotin–fluorescein conjugate. *Biochim. Biophys. Acta* **1427**, 33-43 (1999).
36. Buranda, T. et al. Ligand Receptor Dynamics at Streptavidin-Coated Particle Surfaces: A Flow Cytometric and Spectrofluorimetric Study. *J. Phys. Chem. B* **103**, 3399-3410 (1999).
37. Hoylaerts, M.F., Ding, L., Narisawa, S., Van Kerckhoven, S. & Millán, J.L. Mammalian alkaline phosphatase catalysis requires active site structure stabilization via the N-terminal amino acid microenvironment. *Biochemistry* **45**, 9756-9766 (2006).
38. Sjöback, R., Nygren, J. & Kubista, M. Absorption and fluorescence properties of fluorescein. *Spectrochim. Acta A* **51**, L7-L21 (1995).
39. Cooksey, C. Quirks of dye nomenclature. 9. Fluorescein. *Biotech. Histochem.* **92**, 506-512 (2017).
40. Gracie, K. et al. Interaction of fluorescent dyes with DNA and spermine using fluorescence spectroscopy. *Analyst* **139**, 3735-3743 (2014).
41. Stennett, E.M.S., Ciuba, M.A. & Levitus, M. Photophysical processes in single molecule organic fluorescent probes. *Chem. Soc. Rev.* **43**, 1057-1075 (2014).

42. Marr III, H.E., Stewart, J.M. & Chiu, M.F. The crystal structure of methylene blue pentahydrate. *Acta Cryst. B* **29**, 847-853 (1973).
43. Hähner, G., Marti, A., Spencer, N.D. & Caseri, W.R. Orientation and electronic structure of methylene blue on mica: A near edge x-ray absorption fine structure spectroscopy study. *J. Chem. Phys.* **104**, 7749-7757 (1996).
44. Zanetti-Domingues, L.C., Tynan, C.J., Rolfe, D.J., Clarke, D.T. & Martin-Fernandez, M. Hydrophobic fluorescent probes introduce artifacts into single molecule tracking experiments due to non-specific binding. *PLoS One* **8**, e74200 (2013).
45. Honarmand Ebrahimi, K., Hagedoorn, P.-L., Jacobs, D. & Hagen, W.R. Accurate label-free reaction kinetics determination using initial rate heat measurements. *Sci. Rep.* **5**, 16380 (2015).
46. Iyer, A., Chandra, A. & Swaminathan, R. Hydrolytic enzymes conjugated to quantum dots mostly retain whole catalytic activity. *Biochim. Biophys. Acta, Gen. Subj.* **1840**, 2935-2943 (2014).
47. Jouzi, M., Kerby, M.B., Tripathi, A. & Xu, J. Nanoneedle Method for High-Sensitivity Low-Background Monitoring of Protein Activity. *Langmuir* **24**, 10786-10790 (2008).
48. Di Trani, J.M., Moitessier, N. & Mittermaier, A.K. Complete Kinetic Characterization of Enzyme Inhibition in a Single Isothermal Titration Calorimetric Experiment. *Anal. Chem.* **90**, 8430-8435 (2018).
49. Di Trani, J.M., PhD Thesis (McGill University, 2018).
50. Gudjónsdóttir, K. & Ásgeirsson, B. Effects of replacing active site residues in a cold-active alkaline phosphatase with those found in its mesophilic counterpart from Escherichia coli. *FEBS J.* **275**, 117-127 (2008).
51. Mangoni, M.L. et al. Lipopolysaccharide, a key molecule involved in the synergism between temporins in inhibiting bacterial growth and in endotoxin neutralization. *J. Biol. Chem.* **283**, 22907-22917 (2008).
52. González, M. et al. Interaction of Biotin with Streptavidin: Thermostability and Conformational Changes upon Binding. *J. Biol. Chem.* **272**, 11288-11294 (1997).
53. Weber, P.C., Pantoliano, M.W., Simons, D.M. & Salemme, F.R. Structure-Based Design of Synthetic Azobenzene Ligands for Streptavidin. *J. Am. Chem. Soc.* **116**, 2717-2724 (1994).
54. Ghosh, K. et al. Crystal structure of rat intestinal alkaline phosphatase – Role of crown domain in mammalian alkaline phosphatases. *J. Struct. Biol.* **184**, 182-192 (2013).
55. Bortolato, M., Besson, F. & Roux, B. Role of metal ions on the secondary and quaternary structure of alkaline phosphatase from bovine intestinal mucosa. *Proteins* **37**, 310-318 (1999).
56. Kvach, M.V. et al. 5(6)-Carboxyfluorescein Revisited: New Protecting Group, Separation of Isomers, and their Spectral Properties on Oligonucleotides. *Bioconjugate Chem.* **18**, 1691-1696 (2007).
57. Fernley, H. & Walker, P. Studies on alkaline phosphatase. Inhibition by phosphate derivatives and the substrate specificity. *Biochem. J.* **104**, 1011-1018 (1967).
58. Liu, Y. & Schanze, K.S. Conjugated Polyelectrolyte-Based Real-Time Fluorescence Assay for Alkaline Phosphatase with Pyrophosphate as Substrate. *Anal. Chem.* **80**, 8605-8612 (2008).
59. TURNER, J. Pyridoxal phosphate breakdown by an alkaline-phosphatase preparation. *Biochem. J.* **80**, 663-668 (1961).
60. Coburn, S.P., Mahuren, J.D., Jain, M., Zubovic, Y. & Wortsman, J. Alkaline Phosphatase (EC 3.1.3.1) in Serum Is Inhibited by Physiological Concentrations of Inorganic Phosphate1. *J. Clin. Endocrinol. Metab.* **83**, 3951-3957 (1998).
61. Stinson, R.A. & Seargeant, L.E. Comparative studies of pure alkaline phosphatases from five human tissues. *Clin. Chim. Acta* **110**, 261-272 (1981).
62. Chappelet-Tordo, D., Fosset, M., Iwatsubo, M., Gache, C. & Lazdunski, M. Intestinal alkaline phosphatase. Catalytic properties and half of the sites reactivity. *Biochemistry* **13**, 1788-1795 (1974).

63. Palmier, M.O. & Van Doren, S.R. Rapid determination of enzyme kinetics from fluorescence: Overcoming the inner filter effect. *Anal. Biochem.* **371**, 43-51 (2007).
64. Sancenon, V. et al. Development, validation and quantitative assessment of an enzymatic assay suitable for small molecule screening and profiling: A case-study. *Biomol. Detect. Quantif.* **4**, 1-9 (2015).
65. Kiffer-Moreira, T. et al. Catalytic signature of a heat-stable, chimeric human alkaline phosphatase with therapeutic potential. *PLoS One* **9**, e89374 (2014).
66. van Schie, M.M.C.H., Ebrahimi, K.H., Hagen, W.R. & Hagedoorn, P.-L. Fast and accurate enzyme activity measurements using a chip-based microfluidic calorimeter. *Anal. Biochem.* **544**, 57-63 (2018).
67. Ziegler, A.J., Florian, J., Ballicora, M.A. & Herlinger, A.W. Alkaline phosphatase inhibition by vanadyl-β-diketone complexes: electron density effects. *J. Enzyme Inhib. Med. Chem.* **24**, 22-28 (2009).
68. Jain, M., Vaze, R.G., Ugrani, S.C. & Sharma, K.P. Mechanoresponsive and recyclable biocatalytic sponges from enzyme-polymer surfactant conjugates and nanoparticles. *RSC Adv.* **8**, 39029-39038 (2018).
69. Finkler, B. et al. Monomolecular pyrenol-derivatives as multi-emissive probes for orthogonal reactivities. *Photochem. Photobiol. Sci.* **15**, 1544-1557 (2016).
70. Fernley, H. & Walker, P. Kinetic behaviour of calf-intestinal alkaline phosphatase with 4-methylumbelliferyl phosphate. *Biochem. J.* **97**, 95-103 (1965).
71. Weis, D.D. & Nardozzi, J.D. Enzyme Kinetics in Acoustically Levitated Droplets of Supercooled Water: A Novel Approach to Cryoenzymology. *Anal. Chem.* **77**, 2558-2563 (2005).
72. Lewis, W.H. & Rutan, S.C. Guanidinium-induced differential kinetic denaturation of alkaline phosphatase isozymes. *Anal. Chem.* **63**, 627-629 (1991).
73. Yue, Y.-X. et al. Supramolecular Tandem Assay for Pyridoxal-5 ´ -phosphate by the Reporter Pair of Guanidinocalix[5]Arene and Fluorescein. *ChemistryOpen* **8**, 1437-1440 (2019).
74. Zhu, S. et al. The measurement of cyclic nucleotide phosphodiesterase 4 activities via the quantification of inorganic phosphate with malachite green. *Anal. Chim. Acta* **636**, 105-110 (2009).
75. Chen, J. et al. Real-Time Fluorescence Turn-On Detection of Alkaline Phosphatase Activity with a Novel Perylene Probe. *Chem. Asian J.* **8**, 276-281 (2013).
76. Wang, K., Cui, J.-H., Xing, S.-Y. & Dou, H.-X. A calixpyridinium-based supramolecular tandem assay for alkaline phosphatase and its application to ATP hydrolysis reaction. *Org. Biomol. Chem.* **14**, 2684-2690 (2016).
77. Kearney, A.S. & Stella, V.J. The in Vitro Enzymic Labilities of Chemically Distinct Phosphomonoester Prodrugs. *Pharm. Res.* **9**, 497-503 (1992).
78. Ásgeirsson, B., Hartemink, R. & Chlebowski, J.F. Alkaline phosphatase from Atlantic cod (Gadus morhua). Kinetic and structural properties which indicate adaptation to low temperatures. *Comp. Biochem. Physiol. B* **110**, 315-329 (1995).
79. Motzok, I. & Branion, H.D. Studies on alkaline phosphatases. 2. Factors influencing pH optima and Michaelis constant. *Biochem. J.* **72**, 177-183 (1959).
80. Duncan, P.H., McKneally, S.S., MacNeil, M.L., Fast, D.M. & Bayse, D.D. Development of a reference material for alkaline phosphatase. *Clin. Chem.* **30**, 93-97 (1984).
81. Cathala, G., Brunel, C., Chappelet-Tordo, D. & Lazdunski, M. Bovine kidney alkaline phosphatase. Catalytic properties, subunit interactions in the catalytic process, and mechanism of Mg2+ stimulation. *J. Biol. Chem.* **250**, 6046-6053 (1975).
82. Brunel, C., Cathala, G. & Saintot, M. Purification et propriétés de la phosphatase alcaline du cerveau de bœuf. *Biochim. Biophys. Acta, Enzymol.* **191**, 621-635 (1969).
83. Zittle, C.A. & Bingham, E.W. Action of Purified Milk Phosphatase on Phosphoserine and on Casein. *J. Dairy Sci.* **42**, 1772-1780 (1959).

84. Kumon, A., Kodama, H., Kondo, M., Yokoi, F. & Hiraishi, H. Nω-Phosphoarginine Phosphatase (17 kDa) and Alkaline Phosphatase as Protein Arginine Phosphatases. *J. Biochem.* **119**, 719-724 (1996).
85. Narayanan, S. & Appleton, H.D. Specificity studies on human intestinal alkaline phosphatase. *Biochim. Biophys. Acta* **284**, 175-182 (1972).
86. Trubowitz, S., Feldman, D., Morgenstern, S. & Hunt, V. The isolation, purification and some properties of the alkaline phosphatase of human leucocytes. *Biochem. J.* **80**, 369-374 (1961).
87. Smith, G.P. & Peters, T.J. Purification and properties of alkaline phosphatase from human polymorphonuclear leukocytes. *Int. J. Biochem.* **17**, 209-215 (1985).
88. Harkness, D.R. Studies on human placental alkaline phosphatase: II. Kinetic properties and studies on the apoenzyme. *Arch. Biochem. Biophys.* **126**, 513-523 (1968).
89. Eaton, R.H. & Moss, D.W. Organic pyrophosphates as substrates for human alkaline phosphatases. *Biochem. J.* **105**, 1307-1312 (1967).
90. Wennberg, C. et al. Structure, genomic DNA typing, and kinetic characterization of the D allozyme of placental alkaline phosphatase (PLAP/ALPP). *Hum. Mutat.* **19**, 258-267 (2002).
91. Hiwada, K. & Wachsmuth, E.D. Catalytic properties of alkaline phosphatase from pig kidney. *Biochem. J.* **141**, 283-291 (1974).
92. Harada, T. et al. Characterization of structural and catalytic differences in rat intestinal alkaline phosphatase isozymes. *FEBS J.* **272**, 2477-2486 (2005).
93. Simão, A.M.S. et al. Membrane-bound alkaline phosphatase from ectopic mineralization and rat bone marrow cell culture. *Comp. Biochem. Physiol. A: Mol. Integr. Physiol.* **146**, 679-687 (2007).
94. Müller, K., Schellenberger, V., Borneleit, P. & Treide, A. The alkaline phosphatase from bone: transphosphorylating activity and kinetic mechanism. *Biochim. Biophys. Acta, Protein Struct. Mol. Enzymol.* **1076**, 308-313 (1991).
95. Saini, P.K. & Done, J. The diversity of alkaline phosphatase from rat intestine: Isolation and purification of the enzyme(s). *Biochim. Biophys. Acta, Enzymol.* **258**, 147-153 (1972).
96. Rindi, G., Ricci, V., Gastaldi, G. & Patrini, C. Intestinal Alkaline Phosphatase can Transphosphorylate Thiamin to Thiamin Monophosphate During Intestinal Transport in the Rat. *Arch. Physiol. Biochem.* **103**, 33-38 (1995).
97. Murdoch, R., E Buxton, L. & Kay, D. Mouse Uterine Alkaline Phosphatase: Improved Purification by Affinity Chromatography and Further Characterization of the Enzyme. *Aust. J. Biol. Sci.* **33**, 279-294 (1980).
98. van Belle, H. Kinetics and inhibition of alkaline phosphatases from canine tissues. *Biochim. Biophys. Acta, Enzymol.* **289**, 158-168 (1972).
99. Baracchini Buainain, L., Kimiko Kadowaki, M., de Lourdes Polizeli, M., Francisco Terenzi, H. & Atilio Jorge, J. Characterization of a conidial alkaline phosphatase from the thermophilic fungus Humicola grisea var. thermoidea. *J. Basic Microbiol.* **38**, 85-94 (1998).
100. Lee, D.-H. et al. A novel psychrophilic alkaline phosphatase from the metagenome of tidal flat sediments. *BMC Biotechnol.* **15**, 1 (2015).
101. Ezawa, T., Kuwahara, S.-y., Sakamoto, K., Yoshida, T. & Saito, M. Specific inhibitor and substrate specificity of alkaline phosphatase expressed in the symbiotic phase of the arbuscular mycorrhizal fungus, Glomus etunicatum. *Mycologia* **91**, 636-641 (1999).
102. Fernandez, M.P., Gascon, S. & Schwencke, J. Some enzymatic properties of vacuolar alkaline phosphatase from yeast. *Curr. Microbiol.* **6**, 121-126 (1981).
103. Tuleva, B., Vasileva-Tonkova, E. & Galabova, D. A specific alkaline phosphatase from Saccharomyces cerevisiae with protein phosphatase activity. *FEMS Microbiol. Lett* **161**, 139-144 (1998).
104. Xie, E., Su, Y., Deng, S., Kontopyrgou, M. & Zhang, D. Significant influence of phosphorus resources on the growth and alkaline phosphatase activities of Microcystis aeruginosa. *Environ. Pollut.* **268**, 115807 (2021).

105. Adler, L. Properties of alkaline phosphatase of the halotolerant yeast Debaryomyces hansenii. *Biochim. Biophys. Acta, Enzymol.* **522**, 113-121 (1978).
106. de Oliveira Ornela, P.H. & Guimarães, L.H.S. Purification and characterization of an iron-activated alkaline phosphatase produced by Rhizopus microsporus var. microsporus under submerged fermentation using rye flour. *J. Appl. Biol. Biotech.* **8**, 16-25 (2020).
107. Golotin, V., Balabanova, L., Likhatskaya, G. & Rasskazov, V. Recombinant Production and Characterization of a Highly Active Alkaline Phosphatase from Marine Bacterium Cobetia marina. *Mar. Biotechnol.* **17**, 130-143 (2015).
108. Meng, D. et al. An alkaline phosphatase from Bacillus amyloliquefaciens YP6 of new application in biodegradation of five broad-spectrum organophosphorus pesticides. *J. Environ. Sci. Health B* **54**, 336-343 (2019).
109. Hjörleifsson, J.G. & Ásgeirsson, B. pH-Dependent Binding of Chloride to a Marine Alkaline Phosphatase Affects the Catalysis, Active Site Stability, and Dimer Equilibrium. *Biochemistry* **56**, 5075-5089 (2017).
110. Claussen, J.C. et al. Probing the Enzymatic Activity of Alkaline Phosphatase within Quantum Dot Bioconjugates. *J. Phys. Chem. C* **119**, 2208-2221 (2015).
111. Zhang, R.-Q. et al. Inhibition kinetics of green crab (Scylla serrata) alkaline phosphatase by zinc ions: a new type of complexing inhibition. *Biochim. Biophys. Acta, Protein Struct. Mol. Enzymol.* **1545**, 6-12 (2001).
112. Pétursson, B., BSc Thesis (University of Iceland, 2014).
113. Stankiewicz, P.J. & Gresser, M.J. Inhibition of phosphatase and sulfatase by transition-state analogs. *Biochemistry* **27**, 206-212 (1988).
114. Böger, B. et al. Inhibition of the activated sludge-associated enzyme phosphatase by transition metal oxyanions. *Water Sci. Technol.* **83**, 2629-2639 (2021).
115. Hsu, S.Y. & Goetz, F.W. Oxoanions stimulate in vitro ovulation and signal transduction pathways in goldfish (Carassius auratus) follicles. *Am. J. Physiol. Endocrinol. Metab.* **263**, E943-E949 (1992).
116. Koncki, R., Rudnicka, K. & Tymecki, Ł. Flow injection system for potentiometric determination of alkaline phosphatase inhibitors. *Anal. Chim. Acta* **577**, 134-139 (2006).
117. Reker, C.E., Lapointe, M.C., Kovačič-Milivojević, B., Chiou, W.J.H. & Vedeckis, W.V. A possible role for dephosphorylation in glucocorticoid receptor transformation. *J. Steroid Biochem.* **26**, 653-665 (1987).
118. Whisnant, A.R. & Gilman, S.D. Studies of reversible inhibition, irreversible inhibition, and activation of alkaline phosphatase by capillary electrophoresis. *Anal. Biochem.* **307**, 226-234 (2002).
119. Morton, R.K. The substrate specificity and inhibition of alkaline phosphatases of cow's milk and calf intestinal mucosa. *Biochem. J.* **61**, 232-240 (1955).
120. Murakami, M. Equine Alkaline Phosphatase: III. Some Biochemical Properties of Equine Plasma Alkaline Phosphatase. *Exp. Rep. Equine Hlth. Lab.* **1971**, 110-125 (1971).
121. Cyboron, G., Vejins, M. & Wuthier, R. Activity of epiphyseal cartilage membrane alkaline phosphatase and the effects of its inhibitors at physiological pH. *J. Biol. Chem.* **257**, 4141-4146 (1982).
122. Stec, B., Holtz, K.M. & Kantrowitz, E.R. A revised mechanism for the alkaline phosphatase reaction involving three metal ions. *J. Mol. Biol.* **299**, 1303-1311 (2000).
123. Kim, E.E. & Wyckoff, H.W. Reaction mechanism of alkaline phosphatase based on crystal structures: Two-metal ion catalysis. *J. Mol. Biol.* **218**, 449-464 (1991).
124. Le Du, M.H., Stigbrand, T., Taussig, M.J., Ménez, A. & Stura, E.A. Crystal Structure of Alkaline Phosphatase from Human Placenta at 1.8 Å Resolution: IMPLICATION FOR A SUBSTRATE SPECIFICITY. *J. Biol. Chem.* **276**, 9158-9165 (2001).
125. de Backer, M. et al. The 1.9Å Crystal Structure of Heat-labile Shrimp Alkaline Phosphatase. *J. Mol. Biol.* **318**, 1265-1274 (2002).
126. Ásgeirsson, B., Markússon, S., Hlynsdóttir, S.S., Helland, R. & Hjörleifsson, J.G. X-ray crystal structure of Vibrio alkaline phosphatase with the non-competitive inhibitor cyclohexylamine. *Biochem. Biophys. Rep.* **24**, 100830 (2020).

127. Wende, A. et al. Structural and Biochemical Characterization of a Halophilic Archaeal Alkaline Phosphatase. *J. Mol. Biol.* **400**, 52-62 (2010).
128. Holtz, K.M., Stec, B. & Kantrowitz, E.R. A Model of the Transition State in the Alkaline Phosphatase Reaction. *J. Biol. Chem.* **274**, 8351-8354 (1999).
129. Peck, A., Sunden, F., Andrews, L.D., Pande, V.S. & Herschlag, D. Tungstate as a Transition State Analog for Catalysis by Alkaline Phosphatase. *J. Mol. Biol.* **428**, 2758-2768 (2016).
130. Bessey, O.A., Lowry, O.H. & Brock, M.J. A method for the rapid determination of alkaline phosphatase with five cubic millimeters of serum. *J. Biol. Chem.* **164**, 321-329 (1946).
131. Gee, K.R. et al. Fluorogenic Substrates Based on Fluorinated Umbelliferones for Continuous Assays of Phosphatases and β-Galactosidases. *Anal. Biochem.* **273**, 41-48 (1999).
132. Dong, L., Miao, Q., Hai, Z., Yuan, Y. & Liang, G. Enzymatic Hydrogelation-Induced Fluorescence Turn-Off for Sensing Alkaline Phosphatase in Vitro and in Living Cells. *Anal. Chem.* **87**, 6475-6478 (2015).
133. Song, Z. et al. A Ratiometric Fluorescent Probe Based on ESIPT and AIE Processes for Alkaline Phosphatase Activity Assay and Visualization in Living Cells. *ACS Appl. Mater. Interfaces* **6**, 17245-17254 (2014).
134. Deng, J., Yu, P., Wang, Y. & Mao, L. Real-time Ratiometric Fluorescent Assay for Alkaline Phosphatase Activity with Stimulus Responsive Infinite Coordination Polymer Nanoparticles. *Anal. Chem.* **87**, 3080-3086 (2015).
135. Hou, X., Yu, Q., Zeng, F., Ye, J. & Wu, S. A ratiometric fluorescent probe for in vivo tracking of alkaline phosphatase level variation resulting from drug-induced organ damage. *J. Mater. Chem. B* **3**, 1042-1048 (2015).
136. Zhang, X. et al. A high-sensitivity fluorescent probe with a self-immolative spacer for real-time ratiometric detection and imaging of alkaline phosphatase activity. *New J. Chem.* **43**, 11887-11892 (2019).
137. Zhang, P., Fu, C., Zhang, Q., Li, S. & Ding, C. Ratiometric Fluorescent Strategy for Localizing Alkaline Phosphatase Activity in Mitochondria Based on the ESIPT Process. *Anal. Chem.* **91**, 12377-12383 (2019).
138. Zhao, L. et al. Ratiometric fluorescent response of electrospun fibrous strips for real-time sensing of alkaline phosphatase in serum. *Biosens. Bioelectron.* **91**, 217-224 (2017).
139. Tian, M. et al. Design of ratiometric monoaromatic fluorescence probe via modulating intramolecular hydrogen bonding: A case study of alkaline phosphatase sensing. *Anal. Chim. Acta* **1143**, 144-156 (2021).
140. Liu, H.-W. et al. In Situ Localization of Enzyme Activity in Live Cells by a Molecular Probe Releasing a Precipitating Fluorochrome. *Angew. Chem. Int. Ed.* **56**, 11788-11792 (2017).
141. Kim, T.-I., Kim, H., Choi, Y. & Kim, Y. A fluorescent turn-on probe for the detection of alkaline phosphatase activity in living cells. *Chem. Commun.* **47**, 9825-9827 (2011).
142. Park, J. & Kim, Y. An improved fluorogenic substrate for the detection of alkaline phosphatase activity. *Bioorg. Med. Chem. Lett.* **23**, 2332-2335 (2013).
143. Tan, Y. et al. Reaction-Based Off–On Near-infrared Fluorescent Probe for Imaging Alkaline Phosphatase Activity in Living Cells and Mice. *ACS Appl. Mater. Interfaces* **9**, 6796-6803 (2017).
144. Liu, H.-W. et al. In vivo imaging of alkaline phosphatase in tumor-bearing mouse model by a promising near-infrared fluorescent probe. *Talanta* **175**, 421-426 (2017).
145. Li, S.-J. et al. Facile and Sensitive Near-Infrared Fluorescence Probe for the Detection of Endogenous Alkaline Phosphatase Activity In Vivo. *Anal. Chem.* **89**, 6854-6860 (2017).
146. Liang, J., Kwok, R.T.K., Shi, H., Tang, B.Z. & Liu, B. Fluorescent Light-up Probe with Aggregation-Induced Emission Characteristics for Alkaline Phosphatase Sensing and Activity Study. *ACS Appl. Mater. Interfaces* **5**, 8784-8789 (2013).
147. Paragas, V.B., Zhang, Y.-Z., Haugland, R.P. & Singer, V.L. The ELF-97 Alkaline Phosphatase Substrate Provides a Bright, Photostable, Fluorescent Signal Amplification Method for FISH. *J. Histochem. Cytochem.* **45**, 345-357 (1997).

148. Zhou, W. et al. Self-Cleavable Bioluminogenic Luciferin Phosphates as Alkaline Phosphatase Reporters. *ChemBioChem* **9**, 714-718 (2008).
149. Levine, M.N. & Raines, R.T. Sensitive fluorogenic substrate for alkaline phosphatase. *Anal. Biochem.* **418**, 247-252 (2011).
150. Zhang, H. et al. Construction of an alkaline phosphatase-specific two-photon probe and its imaging application in living cells and tissues. *Biomaterials* **140**, 220-229 (2017).
151. Freeman, R., Finder, T., Gill, R. & Willner, I. Probing Protein Kinase (CK2) and Alkaline Phosphatase with CdSe/ZnS Quantum Dots. *Nano Lett.* **10**, 2192-2196 (2010).
152. Sun, J., Zhao, J., Bao, X., Wang, Q. & Yang, X. Alkaline Phosphatase Assay Based on the Chromogenic Interaction of Diethanolamine with 4-Aminophenol. *Anal. Chem.* **90**, 6339-6345 (2018).
153. Lu, F. et al. Colorimetric alkaline phosphatase activity detection by integrating phosphorylation-mediated sulfydryl protection/deprotection and fluorosurfactant stabilized gold nanoparticles. *Sens. Actuators B Chem.* **325**, 128959 (2020).
154. Tanaka, K., Kitamura, N. & Chujo, Y. Bimodal Quantitative Monitoring for Enzymatic Activity with Simultaneous Signal Increases in 19F NMR and Fluorescence Using Silica Nanoparticle-Based Molecular Probes. *Bioconjugate Chem.* **22**, 1484-1490 (2011).
155. Daryaei, I., Mohammadebrahim Ghaffari, M., Jones, K.M. & Pagel, M.D. Detection of Alkaline Phosphatase Enzyme Activity with a CatalyCEST MRI Biosensor. *ACS Sens.* **1**, 857-861 (2016).
156. Sanzhaeva, U. et al. Imaging of Enzyme Activity by Electron Paramagnetic Resonance: Concept and Experiment Using a Paramagnetic Substrate of Alkaline Phosphatase. *Angew. Chem. Int. Ed.* **57**, 11701-11705 (2018).
157. Sun, D., Xu, W. & Xu, S. Ultrasensitive Raman sensing of alkaline phosphatase activity in serum based on an enzyme-catalyzed reaction. *Anal. Methods* **11**, 3501-3505 (2019).
158. Ruan, C., Wang, W. & Gu, B. Detection of Alkaline Phosphatase Using Surface-Enhanced Raman Spectroscopy. *Anal. Chem.* **78**, 3379-3384 (2006).
159. Sun, D., Xu, W., Liang, C., Shi, W. & Xu, S. A Smart Surface-Enhanced Resonance Raman Scattering Nanoprobe for Monitoring Cellular Alkaline Phosphatase Activity during Osteogenic Differentiation. *ACS Sens.* (2020).
160. Gyurcsányi, R.E., Bereczki, A., Nagy, G., Neuman, M.R. & Lindner, E. Amperometric microcells for alkaline phosphatase assay. *Analyst* **127**, 235-240 (2002).
161. Szydłowska, D., Campàs, M., Marty, J.-L. & Trojanowicz, M. Catechol monophosphate as a new substrate for screen-printed amperometric biosensors with immobilized phosphatases. *Sens. Actuators B Chem.* **113**, 787-796 (2006).
162. Ciana, L.D., Bernacca, G., Bordin, F., Fenu, S. & Garetto, F. Highly sensitive amperometric measurement of alkaline phosphatase activity with glucose oxidase amplification. *J. Electroanal. Chem.* **382**, 129-135 (1995).
163. Serra, B., Morales, M.D., Reviejo, A.J., Hall, E.H. & Pingarrón, J.M. Rapid and highly sensitive electrochemical determination of alkaline phosphatase using a composite tyrosinase biosensor. *Anal. Biochem.* **336**, 289-294 (2005).
164. Goggins, S., Naz, C., Marsh, B.J. & Frost, C.G. Ratiometric electrochemical detection of alkaline phosphatase. *Chem. Commun.* **51**, 561-564 (2015).
165. Mazzei, F. et al. Alkaline phosphatase inhibition based electrochemical sensors for the detection of pesticides. *J. Electroanal. Chem.* **574**, 95-100 (2004).
166. Schrenkhammer, P., Rosnizeck, I.C., Duerkop, A., Wolfbeis, O.S. & Schäferling, M. Time-Resolved Fluorescence-Based Assay for the Determination of Alkaline Phosphatase Activity and Application to the Screening of Its Inhibitors. *J. Biomol. Screen.* **13**, 9-16 (2008).
167. Qian, Z. et al. Carbon Quantum Dots-Based Recyclable Real-Time Fluorescence Assay for Alkaline Phosphatase with Adenosine Triphosphate as Substrate. *Anal. Chem.* **87**, 2966-2973 (2015).

168. Chen, L., Yang, G., Wu, P. & Cai, C. Real-time fluorescence assay of alkaline phosphatase in living cells using boron-doped graphene quantum dots as fluorophores. *Biosens. Bioelectron.* **96**, 294-299 (2017).
169. Chen, C., Zhao, J., Lu, Y., Sun, J. & Yang, X. Fluorescence Immunoassay Based on the Phosphate-Triggered Fluorescence Turn-on Detection of Alkaline Phosphatase. *Anal. Chem.* **90**, 3505-3511 (2018).
170. Ni, P. et al. Spectrophotometric determination of the activity of alkaline phosphatase and detection of its inhibitors by exploiting the pyrophosphate-accelerated oxidase-like activity of nanoceria. *Microchim. Acta* **186**, 320 (2019).
171. Hou, L. et al. A ratiometric multicolor fluorescence biosensor for visual detection of alkaline phosphatase activity via a smartphone. *Biosens. Bioelectron.* **143**, 111605 (2019).
172. Raj, P. et al. Pyrophosphate Prompted Aggregation-Induced Emission: Chemosensor Studies, Cell Imaging, Cytotoxicity, and Hydrolysis of the Phosphoester Bond with Alkaline Phosphatase. *Eur. J. Inorg. Chem.* **2019**, 628-638 (2019).
173. Zhang, L. et al. Inhibition of dsDNA-Templated Copper Nanoparticles by Pyrophosphate as a Label-Free Fluorescent Strategy for Alkaline Phosphatase Assay. *Anal. Chem.* **85**, 3797-3801 (2013).
174. Ma, J.-L., Yin, B.-C., Wu, X. & Ye, B.-C. Copper-Mediated DNA-Scaffolded Silver Nanocluster On–Off Switch for Detection of Pyrophosphate and Alkaline Phosphatase. *Anal. Chem.* **88**, 9219-9225 (2016).
175. Zhao, W., Chiuman, W., Lam, J.C.F., Brook, M.A. & Li, Y. Simple and rapid colorimetric enzyme sensing assays using non-crosslinking gold nanoparticle aggregation. *Chem. Commun.*, 3729-3731 (2007).
176. Wei, H., Chen, C., Han, B. & Wang, E. Enzyme Colorimetric Assay Using Unmodified Silver Nanoparticles. *Anal. Chem.* **80**, 7051-7055 (2008).
177. Nutiu, R., Yu, J.M.Y. & Li, Y. Signaling Aptamers for Monitoring Enzymatic Activity and for Inhibitor Screening. *ChemBioChem* **5**, 1139-1144 (2004).
178. Chen, C. et al. Fluorescence assay for alkaline phosphatase based on ATP hydrolysis-triggered dissociation of cerium coordination polymer nanoparticles. *Analyst* **143**, 3821-3828 (2018).
179. Ma, C. et al. A terbium chelate based fluorescent assay for alkaline phosphatase in biological fluid. *Sens. Actuators B Chem.* **202**, 683-689 (2014).
180. Liu, Y.-C., Peng, S., Angelova, L., Nau, W.M. & Hennig, A. Label-Free Fluorescent Kinase and Phosphatase Enzyme Assays with Supramolecular Host-Dye Pairs. *ChemistryOpen* **8**, 1350-1354 (2019).
181. Zhou, X., Khusbu, F.Y., Chen, H. & Ma, C. A turn-on fluorescence assay of alkaline phosphatase activity based on an enzyme-triggered conformational switch of G-quadruplex. *Talanta* **208**, 120453 (2020).
182. Liu, Y. et al. Selective Sensing of Phosphorylated Peptides and Monitoring Kinase and Phosphatase Activity with a Supramolecular Tandem Assay. *J. Am. Chem. Soc.* **140**, 13869-13877 (2018).
183. Chen, C. et al. Logically Regulating Peroxidase-Like Activity of Gold Nanoclusters for Sensing Phosphate-Containing Metabolites and Alkaline Phosphatase Activity. *Anal. Chem.* **91**, 15017-15024 (2019).
184. Ames, B.N. in Methods Enzymol., Vol. 8 115-118 (Academic Press, 1966).
185. Baykov, A.A., Evtushenko, O.A. & Avaeva, S.M. A malachite green procedure for orthophosphate determination and its use in alkaline phosphatase-based enzyme immunoassay. *Anal. Biochem.* **171**, 266-270 (1988).
186. Li, H., Sun, Y., Li, Y. & Du, J. Alkaline phosphatase activity assay with luminescent metal organic frameworks-based chemiluminescent resonance energy transfer platform. *Microchem. J.* **160**, 105665 (2021).